



Residual-based closure model for density-stratified incompressible turbulent flows

Lixing Zhu^{a,b,c,1}, Arif Masud^{c,*},²

^a *Laboratory of Nonlinear Mechanics, Institute of Mechanics, Chinese Academy of Sciences, Beijing, 100190, China*

^b *School of Engineering Science, University of Chinese Academy of Sciences, Beijing, 100049, China*

^c *Department of Civil and Environmental Engineering, University of Illinois at Urbana-Champaign, Urbana, IL, 61801, USA*

Received 31 December 2020; received in revised form 11 May 2021; accepted 11 May 2021

Available online 16 August 2021

Abstract

This paper presents a locally and dynamically adaptive residual-based closure model for density stratified incompressible flows. The method is based on the three-level form of the Variational Multiscale (VMS) modeling paradigm applied to the system of incompressible Navier–Stokes equations and an energy conservation equation for the relative temperature field. The velocity, pressure, and relative temperature fields are additively decomposed into overlapping scales which leads to a set of coupled mixed-field sub-problems for the coarse- and the fine-scales. In the hierarchical application of the VMS method, the fine-scale velocity and relative temperature fields are further decomposed, leading to a nested system of two-way coupled fine-scale level-I and level-II variational subproblems. A direct application of bubble functions approach to the fine-scale variational equations helps derive fine-scale models that are nonlinear and time dependent. Embedding the derived model from the level-II variational equation in the level-I variational equation helps stabilize the convection-dominated mixed-field thermodynamic subproblem. Locally resolving the unconstrained level-I variational equation yields the residual-based turbulence model which is a function of the residual of the Euler–Lagrange equations of the conservation of momentum, mass, and energy. The derived model accommodates forward- and back-scatter of energy and entropy and embeds sub-grid scale physics in the computable scales of the problem. The steps of the derivation show that it is essential to apply the concept of scale separation systematically to the coupled system of equations and it is critical to preserve the coupling between flow and thermal phases in the fine-scale variational equations. The method has been implemented with hexahedral and tetrahedral elements with equal order interpolations for the velocity, pressure, and temperature fields. Several canonical flow cases are presented that include Rayleigh–Bénard instability, Rayleigh–Taylor instability, and turbulent plane Couette flow with stable stratification.

© 2021 Elsevier B.V. All rights reserved.

Keywords: Variational multiscale method; Hierarchical methods; Density stratification; Incompressible turbulent flows; Boussinesq approximation

1. Introduction

Stratified incompressible flows are encountered in various natural and engineered fluid flow processes. Examples include atmospheric boundary layers, oceanic circulations, and geophysical flows. The models for stratified flows

* Corresponding author.

E-mail address: amasud@illinois.edu (A. Masud).

¹ Former Graduate Research Assistant.

² Professor of Mechanics and Computations.

are comprised of the incompressible Navier–Stokes (NS) equations, coupled with the conservation form of a scalar field equation, namely, temperature, concentration, or density field. Via Reynolds transport theorem, the conservation equation for the scalar field is written as a hyperbolic partial differential equation (PDE), where the velocity field is furnished by the incompressible Navier–Stokes equations. The variation of the induced scalar field is considered as the Boussinesq buoyancy effect that is embedded in the momentum balance equation. This scalar field in turn appears in the conservation of momentum equation, and therefore it is called an “active” field [1,2] due to the two-way coupled nature of the system. For the general class of problems the scalar field can represent the concentration of chemical constituents in combustion [3], the magnetic field in stellar astrophysics [4], or the temperature field that triggers stratification in natural water bodies (e.g., lake and ocean), etc. In particular, density stratification is the dominant physical process in various natural and environmental applications. Natural plumes [5] due to stratification are widely observed at different scales of space and time, and with different levels of intensities, namely, the eruptions of volcanoes or the sudden release of carbon dioxide bubbles in the lakes. The studies on phytoplankton blooms [6] have revealed that the hydrothermal effect plays a vital role in the stimulation of large reproduction of the microalgae. Another class of environmental flows that involves density stratification is the tropical cyclones wherein the wind induced ocean circulation has a strong correlation with the intensity of the hurricanes [7]. Apart from these environmental or geophysical flows, there are industrial applications of stratification in the storage of heat energy [8]. Consequently, a robust computational model is needed to not only understand the role of density stratification in physical processes, including the production and dissipation of turbulence [9–11], but also in the design of energy-efficient devices.

Numerical methods for simulation of stratified turbulence can be classified as Reynolds-Averaged Navier–Stokes (RANS), large-eddy simulations (LES), and direct numerical simulation (DNS) [12]. LES [1] emerges as a method of choice because of its enhanced accuracy with respect to RANS and its lower cost as compared to DNS, thereby providing a balance between accuracy and computational cost. The closure problem (i.e., the gap between filtered and unfiltered nonlinear convection) for stratified flows is more involved than that in the case of isothermal incompressible flows due to the additional nonlinear convection term in the conservation of energy equation. Besides, stratified turbulence also results in anisotropy at the small-scale level, which has been investigated in the literature via DNS techniques [13–15]. Therefore, isothermal LES models for stratified turbulence need to locally adapt in space and in time to address the anisotropy in the unresolved scales. The dynamic strategy to determine turbulence viscosity, first proposed in [16] for isothermal flows, has been utilized in the modeling of LES of stratified turbulence [17–19]. In this context, adaptive local deconvolution method (ALDM) [18] to construct an efficient scheme for implicit LES, and investigations on appropriate filter scales to capture the fundamental features in stratified turbulence [17] have been pursued. In these works it has been shown that the dynamic strategy can result in a negative value of the Smagorinsky coefficient that may eventually lead to instability in the solution [20]. Another approach has been to use the renormalization group (RNG) theory [21] to derive the turbulent viscosity and diffusivity, and it has been extended from isothermal flows [22] to turbulent thermal convection [23].

Apart from the LES models that are based on the turbulent viscosity, the Variational Multiscale (VMS) framework [24–37] provides an alternate approach to the modeling of turbulence that does not rely on any assumptions on the structure of the unresolved scales. A comprehensive literature review of the VMS method for incompressible turbulent flows is presented in [38]. Recently, the VMS method has been used for the coupled system of incompressible NS equations with an active scalar field [39–43], including stratified turbulence [41], thermal convection [39,42] and particle-laden flows [40,43]. In [40,41] a fine-scale model is presented by modifying the coupling provided by the fine-scale inertia while the advection and diffusion of fine-scale velocity and temperature are left uncoupled. An incompressible turbulence model is directly used in [39] for thermal convection.

In the context of the VMS framework, there are two major classes of fine-scale modeling methods: the Green’s function method [24,25,36,39–41], and the bubble functions method [26,27,33,37,44]. The latter method locally resolves the transient linearized fine-scale sub-problems as a function of the residuals at the preceding levels, and is therefore suitable for the extension of turbulence models to account for local anisotropy in the flow physics. In the present work, a residual-based turbulence model is derived by exploiting the notion of multi-level fine-scale modeling [26,27,34,37,44,45] and VMS method for coupled systems [46,47], which results in a fully-coupled turbulence model for stratified turbulent flows. A significant contribution of the present work is that it presents a systematic procedure for applying residual-based ideas to coupled fine-scale variational formulations, while preserving the coupling between flow and thermal phases at the fine scales.

An outline of the paper is as follows. The coupled system of equations for incompressible fluids with density stratification is presented in Section 2. The multiscale weak form that is derived via hierarchical application of the notion of splitting of scales to the coupled system of equations is presented in Section 3. In Section 4, the fine-scale variational structure is exploited via direct application of the bubble functions approach to derive closed-form expressions for the fine-scale fields that serve as the closure model for stratified turbulence. The fine-scale fields are embedded in the global or coarse-scale variational form and it results in a large-eddy simulation method that is endowed with a locally and dynamically adaptive closure model. Section 5 presents a set of numerical test cases to validate the proposed method and to show its application to a range of density stratified incompressible flow problems. Conclusions are drawn in Section 6.

2. Boussinesq approximation for incompressible flow with density stratification

2.1. Strong form

The influence of the spatio-temporally varying active scalar field (e.g., temperature) $T(\mathbf{x}, t)$ leads to spatio-temporal change in the density $\rho(\mathbf{x}, t)$. In the context of incompressible Newtonian fluids, the effect of density variation is accounted for by introducing a buoyancy force to the momentum balance equation, while the continuity equation takes the form of incompressibility condition. An applied thermal gradient and a local heat source serve as the driving mechanisms for the thermal phase. The equations for density-stratified flows, also known as the Boussinesq equations [48], can be written in an open bounded region $\Omega \subset \mathbb{R}^{n_{sd}}$ as follows

$$\mathbf{u}_{,t} + \mathbf{u} \cdot \nabla \mathbf{u} = -\nabla p + \nabla \cdot (2\nu \nabla^s \mathbf{u}) - \hat{\mathbf{g}} \beta \theta + \mathbf{f}_b \quad \text{in } \Omega \times]0, T[\quad (1)$$

$$\nabla \cdot \mathbf{u} = 0 \quad \text{in } \Omega \times]0, T[\quad (2)$$

$$\theta_{,t} + \mathbf{u} \cdot \nabla \theta - \nabla \cdot (\alpha \nabla \theta) = f \quad \text{in } \Omega \times]0, T[\quad (3)$$

where n_{sd} is the number of space dimensions; \mathbf{u} and p are the velocity and kinematic pressure fields, respectively; $\theta = T - T_0$ is the relative temperature field, T is absolute temperature and T_0 is the reference temperature; ν is the kinematic viscosity of the fluid, β is the thermal expansion coefficient, $\hat{\mathbf{g}}$ is the gravitational acceleration vector, α is thermal diffusivity; \mathbf{f}_b is the non-gravitational body force, and f is the heat source/sink. $\mathbf{u}_{,t} = \partial \mathbf{u} / \partial t$ and $\theta_{,t} = \partial \theta / \partial t$ are the time rate of change of velocity and temperature fields, respectively; $\nabla^s = \frac{1}{2} (\nabla + \nabla^T)$ is the symmetric gradient operator. Eq. (1) is the momentum balance equation with a body force that accounts for the thermal effects, Eq. (2) is the continuity equation that enforces the incompressibility condition, and Eq. (3) is the energy conservation equation written in the form of convection–diffusion of the relative temperature field.

The initial conditions in the domain Ω and boundary conditions on the piecewise smooth domain boundary $\Gamma = \partial \Omega$ are:

$$\mathbf{u}(\mathbf{x}, 0) = \mathbf{u}_0(\mathbf{x}) \quad \text{in } \Omega \times \{0\} \quad (4)$$

$$\theta(\mathbf{x}, 0) = \theta_0(\mathbf{x}) \quad \text{in } \Omega \times \{0\} \quad (5)$$

$$\mathbf{u}(\mathbf{x}, t) = \mathbf{g}_M \quad \text{on } \Gamma_g^M \times]0, T[\quad (6)$$

$$\theta(\mathbf{x}, t) = g_E \quad \text{on } \Gamma_g^E \times]0, T[\quad (7)$$

$$\boldsymbol{\sigma} \cdot \mathbf{n} = (2\nu \nabla^s \mathbf{u} - p \mathbf{I}) \cdot \mathbf{n} = \mathbf{h}_M \quad \text{on } \Gamma_h^M \times]0, T[\quad (8)$$

$$\boldsymbol{\phi} \cdot \mathbf{n} = \alpha \nabla \theta \cdot \mathbf{n} = h_E \quad \text{on } \Gamma_h^E \times]0, T[\quad (9)$$

where \mathbf{u}_0 and θ_0 are the initial conditions for velocity and relative temperature fields, respectively; \mathbf{g}_M and g_E are the Dirichlet boundary conditions for the mechanical and thermal phases; \mathbf{h}_M and h_E are the Neumann boundary conditions for mechanical and thermal phases, respectively. From the perspective of the physics of the problem, \mathbf{g}_M and g_E are the prescribed velocities and temperature fields at the boundary, while \mathbf{h}_M and h_E are the prescribed tractions and thermal fluxes. $\boldsymbol{\sigma}$ is the total stress in the fluid and $\boldsymbol{\phi}$ is the heat flux at the boundary. \mathbf{n} is the unit normal vector at the boundary Γ . Specifically, these boundaries satisfy the following conditions: $\Gamma_g^M \cap \Gamma_h^M = \emptyset$, $\Gamma_g^M \cup \Gamma_h^M = \Gamma$, $\Gamma_g^E \cap \Gamma_h^E = \emptyset$ and $\Gamma_g^E \cup \Gamma_h^E = \Gamma$.

Remark 1. In some presentations of the equations for stratified flows [18,23,48] with a known background temperature gradient (e.g., $\frac{dT}{dh}$), the relative temperature field θ is decomposed into $\frac{dT}{dh}z$ and the variation of temperature $\hat{\theta}$, such that $\hat{\theta} = \theta - \frac{dT}{dh}z$. The form of the momentum balance equation (Eq. (1)) still remains unchanged since the Boussinesq buoyancy corresponding to the former part can be absorbed in the pressure term. However, this decomposition leads to an additional term (e.g., $-\frac{dT}{dh}u_3$) in Eq. (3). The residual-based turbulence model being proposed can also be naturally extended to this form of the governing system of equations.

2.2. Standard weak form

Let $\mathbf{w}(\mathbf{x}) \in \mathcal{W} = (H_0^1(\Omega))^{nsd}$, $q(\mathbf{x}) \in \mathcal{Q} = C^0(\Omega) \cap L^2(\Omega)$ and $\eta(\mathbf{x}) \in \mathcal{H} = H_0^1(\Omega)$ be the weighting functions for velocity \mathbf{u} , kinematic pressure p , and relative temperature θ fields. The standard weak form of the problem is: Find $\mathbf{V} = (\mathbf{u}, p, \theta) \in \mathcal{W}_t \times \mathcal{Q}_t \times \mathcal{H}_t$, such that, $\forall \mathbf{W} = (\mathbf{w}, q, \eta) \in \mathcal{W} \times \mathcal{Q} \times \mathcal{H}$

$$(\mathbf{w}, \mathbf{u}_{,t}) + (\mathbf{w}, \mathbf{u} \cdot \nabla \mathbf{u}) + (\nabla \mathbf{w}, 2\nu \nabla^s \mathbf{u}) - (\nabla \cdot \mathbf{w}, p) + (\mathbf{w}, \hat{\mathbf{g}}\beta\theta) = (\mathbf{w}, \mathbf{h}_M)_{\Gamma_h^M} + (\mathbf{w}, \mathbf{f}_b) \quad (10)$$

$$(q, \nabla \cdot \mathbf{u}) = 0 \quad (11)$$

$$(\eta, \theta_{,t}) + (\eta, \mathbf{u} \cdot \nabla \theta) + (\nabla \eta, \alpha \nabla \theta) = (\eta, h_E)_{\Gamma_h^E} + (\eta, f) \quad (12)$$

where \mathcal{W}_t , \mathcal{Q}_t and \mathcal{H}_t are the time-dependent counterparts of the spaces of weighting functions, respectively; and $(\cdot, \cdot) = \int_{\Omega} (\cdot) d\Omega$ denotes the $L_2(\Omega)$ – inner product. The boundary terms on the right hand side (RHS) of Eqs. (10) and (12) are derived from divergence theorem and applying Neumann boundary conditions Eqs. (8) and (9).

2.3. Residual form

For brevity of discussion on the derivation of the turbulence model, we define the residuals of the governing equations in the strong form as

$$\mathbf{r}_M(\mathbf{u}, p, \theta) = \mathbf{u}_{,t} + \mathbf{u} \cdot \nabla \mathbf{u} + \nabla p - \nabla \cdot (2\nu \nabla^s \mathbf{u}) + \hat{\mathbf{g}}\beta\theta - \mathbf{f}_b \quad (13a)$$

$$\mathbf{r}_C(\mathbf{u}) = \nabla \cdot \mathbf{u} \quad (13b)$$

$$\mathbf{r}_E(\mathbf{u}, \theta) = \theta_{,t} + \mathbf{u} \cdot \nabla \theta - \nabla \cdot (\alpha \nabla \theta) - f \quad (13c)$$

and the residuals of weak form as

$$R_M(\mathbf{w}; \mathbf{u}, p, \theta) = B_M(\mathbf{w}; \mathbf{u}, p, \theta) + T_M(\mathbf{w}; \mathbf{u}; \mathbf{u}) - L_M(\mathbf{w}) \quad (14a)$$

$$R_C(q; \mathbf{u}) = B_C(q; \mathbf{u}) \quad (14b)$$

$$R_E(\eta; \mathbf{u}, \theta) = B_E(\eta; \mathbf{u}, \theta) + T_E(\eta; \mathbf{u}; \theta) - L_E(\eta) \quad (14c)$$

The subscript $(\cdot)_M$, $(\cdot)_C$ and $(\cdot)_E$ denotes the momentum balance, mass conservation and energy conservation, respectively. Linear forms $L_M(\mathbf{w})$ and $L_E(\eta)$, bilinear forms B_M , B_C and B_E and trilinear forms T_M and T_E are defined as follows

$$L_M(\mathbf{w}) = (\mathbf{w}, \mathbf{h}_M)_{\Gamma_h^M} + (\mathbf{w}, \mathbf{f}_b) \quad (15a)$$

$$L_E(\eta) = (\eta, h_E)_{\Gamma_h^E} + (\eta, f) \quad (15b)$$

$$B_M(\mathbf{w}; \mathbf{u}, p, \theta) = (\mathbf{w}, \mathbf{u}_{,t}) + (\nabla \mathbf{w}, 2\nu \nabla^s \mathbf{u}) - (\nabla \cdot \mathbf{w}, p) + (\mathbf{w}, \hat{\mathbf{g}}\beta\theta) \quad (15c)$$

$$B_C(q; \mathbf{u}) = (q, \nabla \cdot \mathbf{u}) \quad (15d)$$

$$B_E(\eta; \theta) = (\eta, \theta_{,t}) + (\nabla \eta, \alpha \nabla \theta) \quad (15e)$$

$$T_M(\mathbf{w}; \mathbf{u}; \mathbf{v}) = (\mathbf{w}, \mathbf{u} \cdot \nabla \mathbf{v}) \quad (15f)$$

$$T_E(\eta; \mathbf{u}; \theta) = (\eta, \mathbf{u} \cdot \nabla \theta) \quad (15g)$$

Employing the definition of residuals and bilinear forms, a concise representation of the Galerkin weak form in Eqs. (10)–(12) is written as follows

$$R_M(\mathbf{w}; \mathbf{u}, p, \theta) + R_C(q; \mathbf{u}) + R_E(\eta; \mathbf{u}, \theta) = 0 \quad (16)$$

2.4. Closure problem for density-stratified flows

Compared to the isothermal incompressible flows, there is one more nonlinear convection term $\mathbf{u} \cdot \nabla \theta$ that appears in the strong form Eq. (3) and weak form Eq. (12) of energy conservation equation. In the context of the conventional LES models, the gap between filtered and unfiltered nonlinear convection terms (i.e., $\mathbf{u} \cdot \nabla \theta$ in Eq. (3) and $\mathbf{u} \cdot \nabla \mathbf{u}$ in Eq. (1)) needs to be closed, which is also known as the ‘‘closure problem’’. Employing the VMS method for the system of weak forms, in the following sections we describe the steps involved in the derivation of the fully coupled residual-based turbulence model for density-stratified flows.

3. The variational multiscale method

An earlier work of the senior author adopted two-level scale split [33] to develop residual-based turbulence model, where the so-called *div*-stabilization term [49] was added to ensure mass conservation at the global level. This however required the stability parameter for this term to be designed based on the derived stability tensor [25,33]. In a subsequent work [26], three-level VMS approach of Masud and Franca [45] was adopted for the Navier–Stokes equations wherein split of pressure field into coarse- and fine-scale pressure resulted in a formulation where solution of the fine-scale continuity equation naturally yielded the *div*-stabilization term. In addition, it also resulted in a clean expression for the corresponding stability parameter.

Following along these lines, the derivation of the method in the present work for density-stratified incompressible fluids is carried out using the hierarchical variational framework. It involves functionals with certain restrictions on the admissible spaces of functions that are dictated by the type of the differential operators as well as the boundary and/or constraint conditions. A hierarchical splitting of scales results in a mathematical form that is free of the restriction on the spaces of functions employed for the various fine-scale fields. Consequently, steps involved in the derivation of the method, and the expression for the structure of the stability tensor, are agnostic to the type and order of the shape functions that are employed for approximating the coarse-scale as well as the fine-scale fields. This generality is essential to establish a formal equivalence between the strong and weak forms of the problem and to show variational consistency of the method which ensures that the exact solution also satisfies the weak or the variational form.

3.1. Variational multiscale decomposition

We discretize the bounded domain Ω into n^{el} non-overlapping element subdomains Ω^e with boundary $\Gamma^e = \partial\Omega^e$, where $e = 1, 2, \dots, n^{\text{el}}$. The union of element interiors is defined as $\Omega' = \bigcup_e^{n^{\text{el}}} \Gamma^e \setminus \Omega$. We introduce the additive decomposition of the unknown fields (\mathbf{u}, p, θ) and their corresponding weighting functions (\mathbf{w}, q, η) as follows.

Additively decomposed solution fields

$$\begin{aligned} \mathbf{u}(\mathbf{x}, t) &= \bar{\mathbf{u}}(\mathbf{x}, t) + \mathbf{u}'(\mathbf{x}, t) \\ p(\mathbf{x}, t) &= \bar{p}(\mathbf{x}, t) + p'(\mathbf{x}, t) \\ \theta(\mathbf{x}, t) &= \bar{\theta}(\mathbf{x}, t) + \theta'(\mathbf{x}, t) \end{aligned} \quad (17)$$

Additively decomposed weighting functions

$$\begin{aligned} \mathbf{w}(\mathbf{x}) &= \bar{\mathbf{w}}(\mathbf{x}) + \mathbf{w}'(\mathbf{x}) \\ q(\mathbf{x}) &= \bar{q}(\mathbf{x}) + q'(\mathbf{x}) \\ \eta(\mathbf{x}) &= \bar{\eta}(\mathbf{x}) + \eta'(\mathbf{x}) \end{aligned} \quad (18)$$

For nonlinear fields this decomposition is to be viewed in the sense of projection. Furthermore, to make the definition of the appropriate spaces of functions precise, $\mathcal{V} = \{\bar{\mathbf{u}}, \bar{p}, \bar{\theta}\} \in \bar{\mathcal{W}}_t \times \bar{\mathcal{Q}}_t \times \bar{\mathcal{H}}_t$ and $\mathcal{V}' = \{\mathbf{u}', p', \theta'\} \in \mathcal{W}'_t \times \mathcal{Q}'_t \times \mathcal{H}'_t$. The corresponding weighting function spaces are the time independent spaces such that $\mathcal{W} = \bar{\mathcal{W}} \oplus \mathcal{W}'$; $\mathcal{Q} = \bar{\mathcal{Q}} \oplus \mathcal{Q}'$ and $\mathcal{H} = \bar{\mathcal{H}} \oplus \mathcal{H}'$.

By substituting the additively decomposed weighting functions defined in Eq. (18) in the standard Galerkin weak form Eq. (16), we have

$$R_M(\bar{\mathbf{w}} + \mathbf{w}'; \mathbf{u}, p, \theta) + R_C(\bar{q} + q'; \mathbf{u}) + R_E(\bar{\eta} + \eta'; \mathbf{u}, \theta) = 0 \quad (19)$$

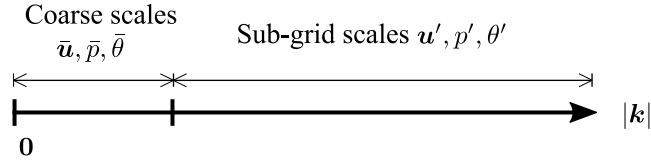


Fig. 1. Two-level scale decomposition along the wave number axis.

Because of the linearity of the additively decomposed weighting functions in Eq. (18), we can split the weak form Eq. (19) into coarse- and fine-scale sub-problems as follows,

Coarse-scale problem

$$R_M(\bar{\mathbf{w}}; \mathbf{u}, p, \theta) + R_C(\bar{q}; \mathbf{u}) + R_E(\bar{\eta}; \mathbf{u}, \theta) = 0 \quad (20)$$

Fine-scale problem

$$R_M(\mathbf{w}'; \mathbf{u}, p, \theta) + R_C(q'; \mathbf{u}) + R_E(\eta'; \mathbf{u}, \theta) = 0 \quad (21)$$

Remark 2. In the context of VMS framework, the basis functions for the coarse-scale trial solutions and weighting functions are viewed as filters or projectors in the conventional LES formulation. Fig. 1 shows the split of scales along the wave number axis $|\mathbf{k}|$.

3.2. Re-organization of the coarse-scale sub-problem

The modeling strategy in Variational Multiscale framework is to extract the fine-scale fields $[\mathbf{u}', p', \theta']$ from fine-scale variational formulation Eq. (21). Subsequently, it is embedded in the coarse-scale formulation Eq. (20) that gives rise to a multiscale weak form with fully embedded VMS-based closure model.

We substitute the additively split trial solutions defined in Eq. (17) in the coarse-scale sub-problem Eq. (20).

$$R_M(\bar{\mathbf{w}}; \bar{\mathbf{u}} + \mathbf{u}', \bar{p} + p', \bar{\theta} + \theta') + R_C(\bar{q}; \bar{\mathbf{u}} + \mathbf{u}') + R_E(\bar{\eta}; \bar{\mathbf{u}} + \mathbf{u}', \bar{\theta} + \theta') = 0 \quad (22)$$

The coarse-scale variational equation in Eq. (22) is expanded out, and the resulting terms are rearranged as follows:

$$B^{\text{Gal}}(\bar{\mathbf{W}}; \bar{\mathbf{V}}) + T^{\text{VMS}}(\bar{\mathbf{W}}; \bar{\mathbf{V}}; \mathbf{V}') + T^{\text{LES}}(\bar{\mathbf{W}}; \mathbf{V}'; \mathbf{V}') = L^{\text{Gal}}(\bar{\mathbf{W}}) \quad (23)$$

where $B^{\text{Gal}}(\bar{\mathbf{W}}; \bar{\mathbf{V}})$ are the bilinear-form terms that are fully represented in terms of coarse-scale fields (i.e., Galerkin terms), $T^{\text{VMS}}(\bar{\mathbf{W}}; \bar{\mathbf{V}}; \mathbf{V}')$ are the trilinear-form terms that linearly depend on the fine-scale trial solution, and $T^{\text{LES}}(\bar{\mathbf{W}}; \mathbf{V}'; \mathbf{V}')$ are the trilinear-form terms that nonlinearly depend on the fine-scale fields. These terms are expressed as

$$B^{\text{Gal}}(\bar{\mathbf{W}}; \bar{\mathbf{V}}) = B_M(\bar{\mathbf{w}}; \bar{\mathbf{u}}, \bar{p}, \bar{\theta}) + T_M(\bar{\mathbf{w}}; \bar{\mathbf{u}}; \bar{\mathbf{u}}) + B_C(\bar{q}; \bar{\mathbf{u}}) + B_E(\bar{\eta}; \bar{\theta}) + T_E(\bar{\eta}; \bar{\mathbf{u}}; \bar{\theta}) \quad (24a)$$

$$T^{\text{VMS}}(\bar{\mathbf{W}}; \bar{\mathbf{V}}; \mathbf{V}') = B_M(\bar{\mathbf{w}}; \mathbf{u}', p', \theta') + T_M(\bar{\mathbf{w}}; \bar{\mathbf{u}}; \mathbf{u}') + T_M(\bar{\mathbf{w}}; \mathbf{u}'; \bar{\mathbf{u}}) + B_C(\bar{q}; \mathbf{u}') \\ + B_E(\bar{\eta}; \theta') + T_E(\bar{\eta}; \bar{\mathbf{u}}; \theta') + T_E(\bar{\eta}; \mathbf{u}'; \bar{\theta}) \quad (24b)$$

$$T^{\text{LES}}(\bar{\mathbf{W}}; \mathbf{V}'; \mathbf{V}') = T_M(\bar{\mathbf{w}}; \mathbf{u}'; \mathbf{u}') + T_E(\bar{\eta}; \bar{\mathbf{u}}'; \theta') \quad (24c)$$

$$L^{\text{Gal}}(\bar{\mathbf{W}}) = L_M(\mathbf{w}) + L_E(\eta) \quad (24d)$$

4. Variational derivation of the closure model

This section presents a systematic procedure for the derivation of the closure model for density-stratified incompressible flows. This derivation relies on consistent linearization of the fine-scale problems, localizing the fine-scale problems to the sum of element interiors, locally resolving for the velocity, pressure and temperature fields at the virtual nodes, and subsequently, re-constructing the element-wise solution fields that constitute the closure model. The model is then embedded in the system of coarse-level variational equations (Eq. (23)). The

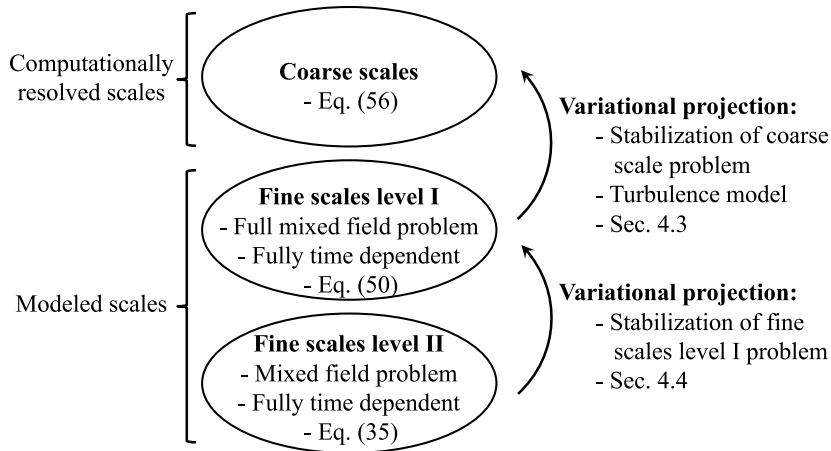


Fig. 2. Schematic diagram of the computed and model scales in the VMS framework.

fine-scale problems summarized in Eq. (21) nevertheless pose the same challenges as the coarse-scale problems, namely, (i) closure problem in the nonlinear convection terms, (ii) restriction imposed by the *inf-sup* condition on the permissible interpolation functions employed in the mixed formulation, and (iii) numerical instability arising due to the convection of fine-scale velocity \mathbf{u}' and relative temperature θ' fields. The first issue is addressed via consistent linearization of the equation, and the second and third issues are resolved through a hierarchical application of VMS idea that results in a nested system of subgrid scale equations that are connected via residuals from the preceding level of scales, as shown in Fig. 2. In the proposed method, the coarse-scale fields are approximated via standard finite element function spaces while the fine-scale fields are approximated with polynomial functions that are independent of the basis-functions employed at the coarse-scale level. These polynomials at the fine scale level also satisfy the property of an interpolation function, assuming a value of 1.0 in the natural coordinates for the internal node and becoming zero at all other nodes. The location of this point in the natural coordinates when projected onto the physical element serves as the position of the virtual node. Since this node is internal to the element, the element level problem can be resolved locally in a variational and analytical context for the coefficients of the fine fields at the virtual node. The analytical expression for the fine-scale solution over element interiors is reconstructed via expansion through the fine-scale functions. This procedure provides some modeling options that can be exploited to simplify the derived expression of the fine scale model and write it in an easy to comprehend form as a function of the residual of element level coarse-scale fields. This step not only yields an analytical expression for the so-called stability tensor, but it also results in economizing the cost of computation of the stability tensor.

4.1. Linearization of the fine-scale problems

The fine-scale problems summarized in Eq. (21) constitute a mixed nonlinear coupled system. The linearization operator is defined as follows.

$$\Pi (R(\mathbf{w}', q', \eta'; \bar{\mathbf{u}}, \mathbf{u}', \bar{p}, p', \bar{\theta}, \theta')) = \frac{d}{d\epsilon} (R(\mathbf{w}', q', \eta'; \bar{\mathbf{u}} + \epsilon\delta\mathbf{u}', \bar{p} + \epsilon\delta p', \bar{\theta} + \epsilon\delta\theta')) \quad (25)$$

Applying this linearization operator to Eq. (21), keeping all the linear terms in the expansion, and grouping the linear terms in the residual forms of conservation of momentum, mass and energy as $\mathcal{L}(R_M(\mathbf{w}'; \bar{\mathbf{u}}, \bar{p}, \bar{\theta}))$, $\mathcal{L}(R_C(q'; \bar{\mathbf{u}}))$, $\mathcal{L}(R_E(\eta'; \bar{\mathbf{u}}, \bar{\theta}))$, respectively, we get the following form.

$$\begin{aligned} &R_M(\mathbf{w}'; \mathbf{u}, p, \theta) + R_C(q'; \mathbf{u}) + R_E(\eta'; \mathbf{u}, \theta) \\ &= R_M(\mathbf{w}'; \bar{\mathbf{u}}, \bar{p}, \bar{\theta}) + R_C(q'; \bar{\mathbf{u}}) + R_E(\eta'; \bar{\mathbf{u}}, \bar{\theta}) + \mathcal{L}(R_M(\mathbf{w}'; \bar{\mathbf{u}}, \bar{p}, \bar{\theta})) + \mathcal{L}(R_C(q'; \bar{\mathbf{u}})) + \mathcal{L}(R_E(\eta'; \bar{\mathbf{u}}, \bar{\theta})) \end{aligned} \quad (26)$$

Employing the bilinear and trilinear operators defined in Eq. (15), the residual form is rearranged into a residual-driven form as follows

$$\begin{aligned} & B_M(\mathbf{w}'; \delta \mathbf{u}', \delta p', \delta \theta') + T_M(\mathbf{w}'; \bar{\mathbf{u}}; \delta \mathbf{u}') + T_M(\mathbf{w}'; \delta \mathbf{u}'; \bar{\mathbf{u}}) \\ & + B_C(q'; \delta \mathbf{u}') + B_E(\eta'; \delta \theta') + T_E(\eta'; \bar{\mathbf{u}}; \delta \theta') + T_E(\eta'; \delta \mathbf{u}'; \bar{\theta}) \\ & = -(\mathbf{w}', \bar{\mathbf{r}}_M) - (q', \bar{r}_C) - (\eta', \bar{r}_E) \end{aligned} \quad (27)$$

where $\bar{\mathbf{r}}_M = \mathbf{r}_M(\bar{\mathbf{u}}, \bar{p}, \bar{\theta})$, $\bar{r}_C = r_C(\bar{\mathbf{u}})$, and $\bar{r}_E = r_E(\bar{\mathbf{u}}, \bar{\theta})$ are the residuals of the Euler–Lagrange equations of the coarse-scale system of conservation of momentum, mass, and energy, respectively.

Remark 3. The linearization process in Eq. (25) eliminates the fine–fine convective term $(\mathbf{w}', \mathbf{u}' \cdot \nabla \mathbf{u}')$ and fine–fine flux $(\eta', \mathbf{u}' \cdot \nabla \theta')$ in a variationally consistent manner, while it preserves the coupling between the mechanical and thermal phases. In the earlier work of the senior author on the derivation of an isothermal incompressible turbulence model [26], a similar treatment was adopted.

Remark 4. To keep the presentation simple and clear, hereon, the notation δ is dropped from the terms containing perturbed fine scales.

4.2. Multiscale decomposition of the fine scales

In Section 3.1, we applied VMS split to the primary fields in the coupled system of equations that is comprised of velocity, pressure, and relative temperature fields. This resulted in a fine-scale system of coupled equations (i.e., Eq. (21)). Since the fine-scale problem is in turn a mixed field problem, therefore locally resolving this system to extract a model for the fine-scale fields still requires that the *inf–sup* restriction on the admissible functions, imposed by the celebrated Babuška–Brezzi (BB) condition, be satisfied. A well-established attribute of the stabilized methods is that they render the discrete formulations free from the restriction imposed by the BB condition, thereby making it convenient to approximate the fields via simpler, and preferably equal-order interpolation functions. Therefore, being able to write the fine-scale problem as a stabilized nonlinear problem would help in extracting the fine-scale model. With this objective of developing a stabilized method at the fine-scale variational level, we proceed with a hierarchical application of the VMS ideas [45] and carry out another split of scales.

In earlier works by the senior author [32,50], it was shown that it may not be necessary to perform scale split for every unknown field in the system to develop the stabilized method. Accordingly, we proceed with splitting only the fine-scale velocity and temperature fields into a set of further finer levels of scales. The rationale to include the temperature field in the subsequent split is that energy conservation equation (i.e., Eq. (3)) is a hyperbolic equation and consequently its fine-scale counterpart requires appropriate stabilization. However, we do not require a further split of the fine-scale pressure. Reason is that localizing the fine-scale fields to element interiors and assuming the fine-scale velocity field to satisfy the Dirichlet boundary condition locally over the element domains results in mass conservation at the fine-scale level, $\int_{\Omega^e} \nabla \cdot \mathbf{u} \, d\Omega = \int_{\Gamma^e} \mathbf{u} \cdot \mathbf{n} \, d\Gamma = 0$. Therefore, further constraint on conservation of mass via split of the pressure field is not needed. Consequently, the structure of the stability tensor contains the basis functions of the fine-scale velocity and temperature fields. Substituting the modeled fine-scale level-II field in the fine-scale level-I problem results in a stabilized fine-scale equation, and therefore the system is free of the restrictions imposed on the admissible spaces of fine-scale basis functions. This flexibility helps in using simple fine-scale basis functions to expand the fields, which facilitates the extracting of analytical expressions for the fine-scale models.

We decompose the fine-scale trial solutions and weighting functions for \mathbf{u}' and θ' into fine-scale level-I and fine-scale level-II. Accordingly, we define the appropriate fine-scale spaces for the velocity and temperature fields such that $\mathcal{W}' = \mathcal{W}'_I \oplus \mathcal{W}'_{II}$ and $\mathcal{H}' = \mathcal{H}'_I \oplus \mathcal{H}'_{II}$. With this decomposition made precise, we now have $\{\mathbf{u}'_I, \theta'_I\} \in \mathcal{W}'_I \times \mathcal{H}'_I$ and $\{\mathbf{u}'_{II}, \theta'_{II}\} \in \mathcal{W}'_{II} \times \mathcal{H}'_{II}$.

$$\mathbf{u}'(\mathbf{x}, t) = \mathbf{u}'_I(\mathbf{x}, t) + \mathbf{u}'_{II}(\mathbf{x}, t) \quad \theta'(\mathbf{x}, t) = \theta'_I(\mathbf{x}, t) + \theta'_{II}(\mathbf{x}, t) \quad (28)$$

$$\mathbf{w}'(\mathbf{x}) = \mathbf{w}'_I(\mathbf{x}) + \mathbf{w}'_{II}(\mathbf{x}) \quad \eta'(\mathbf{x}) = \eta'_I(\mathbf{x}) + \eta'_{II}(\mathbf{x}) \quad (29)$$

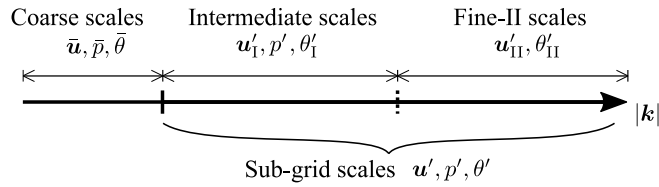


Fig. 3. Three-level scale decomposition along the wave number axis $|k|$.

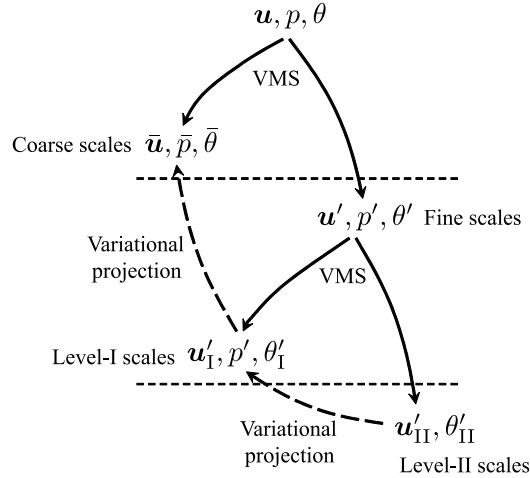


Fig. 4. Schematic diagram of hierarchical separation of scales and bottom-up development of the closure model.

Such a decomposition of fine-scale fields can also be presented in the spectral space, as shown in Fig. 3.

By segregating the terms in the weighting function slot corresponding to the two levels in the fine-scale, we obtain the fine-scale level-I and fine-scale level-II sub-problems.

Fine-Scale Level-I

$$\begin{aligned}
 & B_M(\mathbf{w}'_I; \mathbf{u}', p', \theta') + T_M(\mathbf{w}'_I; \bar{\mathbf{u}}; \mathbf{u}') + T_M(\mathbf{w}'_I; \mathbf{u}'; \bar{\mathbf{u}}) \\
 & + B_C(q'; \mathbf{u}') + B_E(\eta'_I; \theta') + T_E(\eta'_I; \bar{\mathbf{u}}; \theta') + T_E(\eta'_I; \mathbf{u}'; \bar{\theta}) \\
 & = -(\mathbf{w}'_I, \bar{\mathbf{r}}_M) - (q', \bar{r}_C) - (\eta'_I, \bar{r}_E)
 \end{aligned} \tag{30}$$

Fine-Scale Level-II

$$\begin{aligned}
 & B_M(\mathbf{w}'_{II}; \mathbf{u}', p', \theta') + T_M(\mathbf{w}'_{II}; \bar{\mathbf{u}}; \mathbf{u}') + T_M(\mathbf{w}'_{II}; \mathbf{u}'; \bar{\mathbf{u}}) \\
 & + B_E(\eta'_{II}; \theta') + T_E(\eta'_{II}; \bar{\mathbf{u}}; \theta') + T_E(\eta'_{II}; \mathbf{u}'; \bar{\theta}) = -(\mathbf{w}'_{II}, \bar{\mathbf{r}}_M) - (\eta'_{II}, \bar{r}_E)
 \end{aligned} \tag{31}$$

Our aim is to extract the solution of fine-scale level-II velocity \mathbf{u}'_{II} and temperature θ'_{II} fields by locally resolving Eq. (31). These analytical expressions will then be substituted in the fine-scale level-I variational form Eq. (30) and will result in a stabilized formulation for the fine-scale problems. Fig. 4 shows the hierarchical decomposition of scales and the subsequent rebuilding of the fine-scale models that are sequentially embedded in the preceding level variational forms.

Remark 5. The effect of splitting the velocity and not the pressure field is that it results in enriching only the velocity degrees of freedom, which is attractive from the perspective of the notion of the ratio of constraint count, i.e., the ratio of the velocity to the pressure degrees of freedom [51].

4.3. Deriving the model for the fine-scale level-II fields

To make the problems tractable, we make an assumption that the fine-scale fields vanish at the element boundaries.

$$\mathbf{u}' = 0 \quad p' = 0 \quad \theta' = 0 \quad \text{on } \Gamma' \tag{32}$$

$$\mathbf{w}' = 0 \quad q' = 0 \quad \eta' = 0 \quad \text{on } \Gamma' \tag{33}$$

We rearrange the fine-scale terms in Eq. (31) by separating the fine-scale trial solutions that belong to level-II from those at level-I.

$$\begin{aligned} & B_M(\mathbf{w}'_{\Pi}; \mathbf{u}'_{\Pi}, 0, \theta'_{\Pi}) + T_M(\mathbf{w}'_{\Pi}; \bar{\mathbf{u}}; \mathbf{u}'_{\Pi}) + T_M(\mathbf{w}'_{\Pi}; \mathbf{u}'_{\Pi}; \bar{\mathbf{u}}) \\ & + B_E(\eta'_{\Pi}; \theta'_{\Pi}) + T_E(\eta'_{\Pi}; \bar{\mathbf{u}}; \theta'_{\Pi}) + T_E(\eta'_{\Pi}; \mathbf{u}'_{\Pi}; \bar{\theta}) \\ = & -B_M(\mathbf{w}'_{\Pi}; \mathbf{u}'_1, p', \theta'_1) - T_M(\mathbf{w}'_{\Pi}; \bar{\mathbf{u}}; \mathbf{u}'_1) - T_M(\mathbf{w}'_{\Pi}; \mathbf{u}'_1; \bar{\mathbf{u}}) \\ & - B_E(\eta'_{\Pi}; \theta'_1) - T_E(\eta'_{\Pi}; \bar{\mathbf{u}}; \theta'_1) - T_E(\eta'_{\Pi}; \mathbf{u}'_1; \bar{\theta}) - (\mathbf{w}'_{\Pi}, \mathbf{r}_M) - (\eta'_{\Pi}, r_E) \end{aligned} \tag{34}$$

The RHS of the rearranged fine-scale level-II weak form Eq. (34) can be written in the residual-driven form.

$$\begin{aligned} & B_M(\mathbf{w}'_{\Pi}; \mathbf{u}'_{\Pi}, 0, \theta'_{\Pi}) + T_M(\mathbf{w}'_{\Pi}; \bar{\mathbf{u}}; \mathbf{u}'_{\Pi}) + T_M(\mathbf{w}'_{\Pi}; \mathbf{u}'_{\Pi}; \bar{\mathbf{u}}) \\ & + B_E(\eta'_{\Pi}; \theta'_{\Pi}) + T_E(\eta'_{\Pi}; \bar{\mathbf{u}}; \theta'_{\Pi}) + T_E(\eta'_{\Pi}; \mathbf{u}'_{\Pi}; \bar{\theta}) \\ = & -(\mathbf{w}'_{\Pi}, \mathbf{r}'_M + \bar{\mathbf{r}}_M) - (\eta'_{\Pi}, r'_E + \bar{r}_E) \end{aligned} \tag{35}$$

where \mathbf{r}'_M is the residual of the Euler–Lagrange equations of the linearized fine-scale level-I for the conservation of momentum, while r'_E is the residual of the Euler–Lagrange equation of the linearized fine-scale level-I conservation of energy. The expressions for \mathbf{r}'_M and r'_E are as follows

$$\begin{aligned} \mathbf{r}'_M &= \mathbf{u}'_{1,t} + \bar{\mathbf{u}} \cdot \nabla \mathbf{u}'_1 + \mathbf{u}'_1 \cdot \nabla \bar{\mathbf{u}} + \nabla p' - \nabla \cdot (2\nu \nabla \mathbf{u}'_1) - \hat{\mathbf{g}} \beta \theta'_1 \\ r'_E &= \theta'_{1,t} + \bar{\mathbf{u}} \cdot \nabla \theta'_1 + \mathbf{u}'_1 \cdot \nabla \bar{\theta} - \nabla \cdot (\alpha \nabla \theta'_1) \end{aligned} \tag{36}$$

At this point we introduce the notion of bubble functions to expand the fine-scale fields at level-II. These functions, by their definition, vanish at element boundaries and therefore satisfy the assumptions inherent in Eqs. (32) and (33). The interpolation of fine-scale level-II trial solutions and weighting functions are therefore written as follows

$$\mathbf{u}'_{\Pi} = b_{\Pi}^e \mathbf{u}'_{\Pi}{}^e \quad \text{and} \quad \theta'_{\Pi} = b_{\Pi}^e \theta'_{\Pi}{}^e \tag{37}$$

$$\mathbf{w}'_{\Pi} = b_{\Pi}^e \mathbf{w}'_{\Pi}{}^e \quad \text{and} \quad \eta'_{\Pi} = b_{\Pi}^e \eta'_{\Pi}{}^e \tag{38}$$

where the superscript $(\cdot)^e$ in Eqs. (37) and (38) denotes the element-wise quantity. For integration in time, we have employed the generalized- α method [52] for the first-order system, where the inertial term is evaluated at $n + \alpha_m$ while other terms are evaluated at $n + \alpha_f$ over a time-step from time level n to $n + 1$. By applying the spatial discretization in Eqs. (37) and (38) to Eq. (35), we arrive at a linear system

$$\frac{\alpha_m}{\gamma \Delta t} \mathbf{M}'_{\Pi} \begin{bmatrix} \mathbf{u}'_{\Pi,t}{}^e \\ \theta'_{\Pi,t}{}^e \end{bmatrix}_{n+1} + \alpha_f \mathbf{K}'_{\Pi} \begin{bmatrix} \mathbf{u}'_{\Pi}{}^e \\ \theta'_{\Pi}{}^e \end{bmatrix}_{n+1} = -\alpha_f \mathbf{R}'_{\Pi} \begin{bmatrix} \mathbf{r}_M + \mathbf{r}'_M \\ r_E + r'_E \end{bmatrix}_{n+1} \tag{39}$$

where $\mathbf{M}'_{\Pi} = (b^e, b^e) \mathbf{I}_{4 \times 4}$ is the mass matrix of the linear system, and $\mathbf{R}'_{\Pi} = (b^e, 1) \mathbf{I}_{4 \times 4}$ is the matrix comprised of bubble functions, which multiplies the set of residual vectors to yield the out of balance force vector for the evolution of fine scales. The stiffness matrix \mathbf{K}'_{Π} is defined as follows

$$\mathbf{K}'_{\Pi} = \begin{bmatrix} \mathbf{K}_{\Pi}^{w'u'} & \mathbf{K}_{\Pi}^{w'\theta'} \\ \mathbf{K}_{\Pi}^{\eta'u'} & \mathbf{K}_{\Pi}^{\eta'\theta'} \end{bmatrix} \tag{40}$$

where $\mathbf{K}_{\Pi}^{w'u'} = \mathbf{K}_{\text{Gal}}^{w'u'}(b^e)$ and includes the cross-scale advection, skew advection and symmetric diffusion. This in fact constitutes the standard discrete sub-system for the linearized Navier–Stokes equations that is derived in our earlier work [32,46]. $\mathbf{K}_{\Pi}^{\eta'\theta'} = \mathbf{K}_{\text{Gal}}^{\eta'\theta'}(b^e)$ represents the cross-scale advection–diffusion terms in the thermal

phase and is form identical to our earlier work in [46,53]. The coupling terms (i.e., $\mathbf{K}_{\text{II}}^{w'\theta'_I} = \mathbf{K}_{\text{Gal}}^{w'\theta'}(b_{\text{II}}^e)$ and $\mathbf{K}_{\text{II}}^{\eta'_I u'_I} = \mathbf{K}_{\text{Gal}}^{\eta'_I u'_I}(b_{\text{II}}^e)$) of the mechanical phase and the thermal phase also appear in the fine-scale problems. Consequently, a full $(n_{sd} + 1) \times (n_{sd} + 1)$ matrix is derived from the discretized linear system in Eq. (39). Hereon, the fine-scale level-II velocity and temperature fields are written in terms of the residuals of the conservation laws at the preceding levels.

$$\begin{bmatrix} \mathbf{u}'_{\text{II}} \\ \theta'_I \end{bmatrix} = b_{\text{II}}^e \begin{bmatrix} \mathbf{u}'_{\text{II}} \\ \theta'_I \end{bmatrix} = -\boldsymbol{\tau}' \begin{bmatrix} \mathbf{r}_M + \mathbf{r}'_M \\ r_E + r'_E \end{bmatrix} \quad (41)$$

where $\boldsymbol{\tau}'$ represents a local variational projector that maps the solution from the smallest scales (i.e., level-II) to the next larger scales (i.e., level-I). The derived expression of $\boldsymbol{\tau}'$ is

$$\boldsymbol{\tau}' = b_{\text{II}}^e \left(\frac{\alpha_m}{\alpha_f \gamma \Delta t} \mathbf{M}'_{\text{II}} + \mathbf{K}'_{\text{II}} \right)^{-1} \mathbf{R}'_{\text{II}} \quad (42)$$

Remark 6. Further details on the structure of $\boldsymbol{\tau}'$ that can help the interested reader to implement the method are provided in [Appendix A.1](#).

Remark 7. The time-dependent terms $(\cdot)_n$ and their time derivative $\partial(\cdot)_n/\partial t$ for the level-II fine-scale fields are neglected (i.e., $(\cdot)_n = 0$ and $\partial(\cdot)_n/\partial t = 0$). For a generic time-dependent field (\cdot) , the temporal discretization via the generalized- α method can be written as

$$\begin{aligned} \frac{\partial(\cdot)}{\partial t} \Big|_{n+1} &= \frac{(\cdot)_{n+1} - (\cdot)_n}{\gamma \Delta t} + \frac{\gamma - 1}{\gamma} \frac{\partial(\cdot)}{\partial t} \Big|_n = \frac{1}{\gamma \Delta t} (\cdot)_{n+1} \\ \frac{\partial(\cdot)}{\partial t} \Big|_{n+\alpha_m} &= \alpha_m \frac{\partial(\cdot)}{\partial t} \Big|_{n+1} + (1 - \alpha_m) \frac{\partial(\cdot)}{\partial t} \Big|_n = \frac{\alpha_m}{\gamma \Delta t} (\cdot)_{n+1} \\ (\cdot) \Big|_{n+\alpha_f} &= \alpha_f (\cdot) \Big|_{n+1} + (1 - \alpha_f) (\cdot) \Big|_n = \alpha_f (\cdot) \Big|_{n+1} \end{aligned} \quad (43)$$

The value of parameters α_m , α_f and γ that ensure the unconditional stability of the algorithm are determined by the parameter ρ_∞ [52].

Remark 8. To address the issue of orthogonality of standard bubble function and its derivatives, the weighting part of the advection term in Eq. (40) is enriched with advection bubble, as suggested in senior author's earlier work [32,53].

Remark 9. The fine-scale level-II fields are fully cognizant of the residuals at the preceding coarse levels, and these effects are fully embedded in the models for $[\mathbf{u}'_{\text{II}}, \theta'_I]^T$ as derived in Eq. (41).

4.4. Derivation of the closure model

4.4.1. Stabilized fine-scale level-I weak form

To embed the derived fine-scale level-II fields, we first expand the terms in the fine-scale level-I equation (Eq. (30)) by substituting the additively decomposed form Eq. (28). We then group the terms with respect to the two levels in the trial solution slot, which yields

$$B_I^{\text{Gal}}(\mathbf{W}'_I; V'_I) + T_I^{\text{VMS}}(\mathbf{W}'_I; V'_{\text{II}}) = L_I^{\text{RHS}}(\mathbf{W}'_I; \bar{V}) \quad (44)$$

where B_I^{Gal} represents the Galerkin terms that encompass the fine-scale level-I solution fields, T_I^{VMS} constitutes the terms that depend on the fine-scale level-II fields, and it is here that the fine-scale level-II solution from Eq. (41) is substituted. L_I^{RHS} represents the terms that depend on the coarse-scale solution fields. The expressions for these terms are

$$\begin{aligned} B_I^{\text{Gal}}(\mathbf{W}'_I; V'_I) &= B_M(\mathbf{w}'_I; \mathbf{u}'_I, p', \theta'_I) + T_M(\mathbf{w}'_I; \bar{\mathbf{u}}; \mathbf{u}'_I) + T_M(\mathbf{w}'_I; \mathbf{u}'_I; \bar{\mathbf{u}}) \\ &\quad + B_C(q'; \mathbf{u}'_I) + B_E(\eta'_I; \theta'_I) + T_E(\eta'_I; \bar{\mathbf{u}}; \theta'_I) + T_E(\eta'_I; \mathbf{u}'_I; \bar{\theta}) \end{aligned} \quad (45)$$

$$T_I^{\text{VMS}}(\mathbf{W}'_I; \mathbf{V}'_{II}) = B_M(\mathbf{w}'_I; \mathbf{u}'_{II}, 0, \theta'_I) + T_M(\mathbf{w}'_I; \bar{\mathbf{u}}; \mathbf{u}'_{II}) + T_M(\mathbf{w}'_I; \mathbf{u}'_{II}; \bar{\mathbf{u}}) + B_E(\eta'_I; \theta'_I) + T_E(\eta'_I; \bar{\mathbf{u}}; \theta'_I) + T_E(\eta'_I; \mathbf{u}'_{II}; \bar{\theta}) \tag{46}$$

$$L_I^{\text{RHS}}(\mathbf{W}'; \bar{\mathbf{V}}) = -(\mathbf{w}'_I, \bar{\mathbf{r}}_M) - (q', \bar{r}_C) - (\eta'_I, \bar{r}_E) \tag{47}$$

By applying divergence theorem to T_I^{VMS} , we have

$$T_I^{\text{VMS}}(\mathbf{W}'_I; \mathbf{V}'_{II}) = \left([\chi'_M, \chi'_E], [\mathbf{u}'_{II}, \theta'^e_{II}]^T \right) \tag{48}$$

where weighting functions χ'_M and χ'_E are comprised of the various terms that depends on the fine-scale level-II solution in Eq. (46), and are given as follows,

$$\chi'_M = -\bar{\mathbf{u}} \cdot \nabla \mathbf{w}'_I + \mathbf{w}'_I \cdot \nabla^T \bar{\mathbf{u}} - \nu(\nabla(\nabla \cdot \mathbf{w}'_I) + \Delta \mathbf{w}'_I) - \nabla \cdot \mathbf{q}' + \eta'_I \nabla^T \bar{\theta} \tag{49a}$$

$$\chi'_E = \beta \hat{\mathbf{g}} \cdot \mathbf{w}'_I - \bar{\mathbf{u}} \cdot \nabla \eta'_I - \alpha \Delta \eta'_I \tag{49b}$$

We now substitute the fine-scale level-II solution from Eq. (41) in Eq. (48) and take the residual of the coarse-scale Euler–Lagrange equation to the RHS of Eq. (44). The resulting stabilized fine-scale level-I weak form is written as follows

$$B_I^{\text{Gal}}(\mathbf{W}'_I; \mathbf{V}'_I) - ([\chi'_M, \chi'_E] \boldsymbol{\tau}'; [\mathbf{r}'_M, r'_E]^T) = L_I^{\text{RHS}}(\mathbf{W}'; \bar{\mathbf{V}}) - ([\chi'_M, \chi'_E] \boldsymbol{\tau}'; [\bar{\mathbf{r}}'_M, \bar{r}'_E]^T) \tag{50}$$

4.4.2. Solution of fine-scale level-I

The L.H.S. of Eq. (50) depends on the fine-scale level-I trial solutions only, and this is a consequence of the variationally derived models for $[\mathbf{u}'_{II}, \theta'_{II}]^T$ that are written in terms of the residuals at level-I as shown in Eq. (41). We now locally resolve Eq. (50) to derive analytical expressions for $[\mathbf{u}'_I, p', \theta'_I]^T$ in a residual form, as shown on the R.H.S. of Eq. (50). We employ bubble functions b_I^e to interpolate $[\mathbf{u}'_I, p', \theta'_I]^T$ and their corresponding weighting functions $[\mathbf{w}'_I, q', \eta'_I]^T$ as

$$[\mathbf{u}'_I, p', \theta'_I]^T = b_I^e [\mathbf{u}'_I, p', \theta'_I]^T \quad \text{and} \quad [\mathbf{w}'_I, q', \eta'_I]^T = b_I^e [\mathbf{w}'_I, q', \eta'_I]^T \tag{51}$$

It is important to note that bubble function b_I^e is linearly independent of the function b_{II} in Eqs. (28) and (29). We apply the generalized- α method to discretize the system in time. To simplify the equations, we drop the time history terms and employing Eq. (51), the stabilized fine-scale level-I weak form Eq. (50) can be written in an element-wise matrix form as

$$\left(\frac{\alpha_m}{\gamma \Delta t} \mathbf{M}'_I + \alpha_f \mathbf{K}'_I \right) \begin{bmatrix} \mathbf{u}'_I \\ p' \\ \theta'_I \end{bmatrix} = -\alpha_f \mathbf{R}'_I \begin{bmatrix} \bar{\mathbf{r}}_M \\ \bar{r}_C \\ \bar{r}_E \end{bmatrix} \tag{52}$$

where \mathbf{M}'_I is the mass matrix of fine-scale level-I, \mathbf{K}'_I is the stiffness matrix, and \mathbf{R}'_I is the RHS matrix. Locally solving Eq. (52) over the element interiors with an appropriate time integration scheme gives the coefficients for $[\mathbf{u}'_I, p', \theta'_I]^T$ at the virtual nodes. We can reconstruct the fine-scale fields by multiplying with the bubble function. The fine-scale level-I represents the closure model for the fine-scales where physics from higher modes (i.e., finer scales) has been embedded via nesting through the hierarchical residuals. We denote the solution of the fine-scale system in Eq. (52) as

$$\begin{bmatrix} \mathbf{u}' \\ p' \\ \theta' \end{bmatrix} \approx \begin{bmatrix} \mathbf{u}'_I \\ p' \\ \theta'_I \end{bmatrix} = b_I^e \begin{bmatrix} \mathbf{u}'_I \\ p' \\ \theta'_I \end{bmatrix} = -b^e \boldsymbol{\tau} \begin{bmatrix} \mathbf{r}_M \\ r_C \\ r_E \end{bmatrix} \tag{53}$$

where $\boldsymbol{\tau}$ projects fine-scale physics from sub-grid scales to the resolved scales, viz.,

$$\boldsymbol{\tau} = b_I^e \left(\frac{\alpha_m}{\alpha_f \gamma \Delta t} \mathbf{M}'_I + \mathbf{K}'_I \right)^{-1} \mathbf{R}'_I \tag{54}$$

Remark 10. The structure of $\boldsymbol{\tau}$ along with the algorithmic detail for its numerical implementation are provided in Appendix A.2.

4.5. Residual-based turbulence model

We recall the coarse-scale problem defined in Eq. (23), substitute the scale decomposition of the trial solutions, and write out the terms

$$(\bar{\mathbf{w}}, \bar{\mathbf{u}}_{,t}) + (\bar{\mathbf{w}}, \bar{\mathbf{u}} \cdot \nabla \bar{\mathbf{u}}) + (\nabla \bar{\mathbf{w}}, 2\nu \nabla^s \bar{\mathbf{u}}) - (\nabla \cdot \bar{\mathbf{w}}, \bar{p}) + (\bar{\mathbf{w}}, \hat{\mathbf{g}} \beta \bar{\theta}) \quad (55a)$$

$$+ (\bar{q}, \nabla \cdot \bar{\mathbf{u}}) \quad (55b)$$

$$+ (\bar{\eta}, \bar{\theta}_{,t}) + (\bar{\eta}, \bar{\mathbf{u}} \cdot \nabla \bar{\theta}) + (\nabla \bar{\eta}, \alpha \nabla \bar{\theta}) \quad (55c)$$

$$+ (\bar{\mathbf{w}}, \mathbf{u}'_{,t}) + (\bar{\mathbf{w}}, \bar{\mathbf{u}} \cdot \nabla \mathbf{u}') + (\bar{\mathbf{w}}, \mathbf{u}' \cdot \nabla \bar{\mathbf{u}}) + (\nabla \bar{\mathbf{w}}, 2\nu \nabla^s \mathbf{u}') + (\bar{q}, \nabla \cdot \mathbf{u}') \quad (55d)$$

$$- (\nabla \cdot \bar{\mathbf{w}}, p') \quad (55e)$$

$$+ (\bar{\eta}, \theta'_{,t}) + (\bar{\eta}, \bar{\mathbf{u}} \cdot \nabla \theta') + (\nabla \bar{\eta}, \alpha \nabla \theta') \quad (55f)$$

$$+ (\bar{\mathbf{w}}, \hat{\mathbf{g}} \beta \theta') + (\bar{\eta}, \mathbf{u}' \cdot \nabla \bar{\theta}) \quad (55g)$$

$$+ (\bar{\mathbf{w}}, \mathbf{u}' \cdot \nabla \mathbf{u}') + (\bar{\eta}, \mathbf{u}' \cdot \nabla \theta') = 0 \quad (55h)$$

The description of these terms is as follows: (i) the terms in Eq. (55a) constitute the coarse-scale Galerkin form of the momentum balance equation $R_M(\bar{\mathbf{w}}; \bar{\mathbf{u}}, \bar{p}, \bar{\theta})$, (ii) the term in Eq. (55b) is the coarse-scale Galerkin form of the continuity equation $R_C(\bar{q}; \bar{\mathbf{u}})$, (iii) the terms in Eq. (55c) are the coarse-scale Galerkin form of the energy conservation equation $R_E(\bar{\eta}; \bar{\mathbf{u}}, \bar{\theta})$, (iv) the terms in Eq. (55d) are VMS terms from the mechanical phase (and these terms are grouped as (χ_M, \mathbf{u}') via integration by parts), (v) Eq. (55e) is the VMS term with respect to fine-scale pressure p' (and it encompasses the so-called *div*-stabilization), (vi) the terms in Eq. (55f) are the VMS terms from thermal phase (and we can rewrite them as (χ_E, θ')), (vii) the terms in Eq. (55g) represent the inter-scale and inter-phase coupling, namely, the effect of fine-scale temperature on the coarse-scale mechanical phase, and the effect of fine-scale velocity on the coarse-scale thermal phase, and (viii) the terms in Eq. (55h) are higher-order fine scale convection terms.

Remark 11. In Eqs. (55d) and (55f), we have dropped $(\bar{\mathbf{w}}, \mathbf{u}'_{,t})$ and $(\bar{\eta}, \theta'_{,t})$ because fine-scale dynamic effects have been implicitly represented via embedding of fine-scale models in the coarse-scale variational equation. This also helps simplify numerical solution algorithm for the coarse-scale formulation, while still maintaining the dependency of the stability tensor on the time-evolving fine scales.

The residual-based turbulence formulation can be written in a concise form as:

$$\boxed{R_M(\bar{\mathbf{w}}; \bar{\mathbf{u}}, \bar{p}, \bar{\theta}) + R_C(\bar{q}; \bar{\mathbf{u}}) + R_E(\bar{\eta}; \bar{\mathbf{u}}, \bar{\theta}) + (\chi_M, \mathbf{u}') - (\nabla \cdot \bar{\mathbf{w}}, p') + (\chi_E, \theta') + (\bar{\mathbf{w}}, \mathbf{u}' \cdot \nabla \mathbf{u}') + (\bar{\eta}, \mathbf{u}' \cdot \nabla \theta') = 0} \quad (56)$$

where the closure model $[\mathbf{u}', p', \theta']^T$ is derived in Eq. (53). The weighting functions χ_M and χ_E that correspond to the stabilization terms are written as

$$\begin{aligned} \chi_M &= -\bar{\mathbf{u}} \cdot \nabla \bar{\mathbf{w}} + \bar{\mathbf{w}} \cdot \nabla^T \bar{\mathbf{u}} - \nu(\nabla(\nabla \cdot \bar{\mathbf{w}}) + \Delta \bar{\mathbf{w}}) - \nabla \cdot q + \bar{\eta} \cdot \nabla^T \bar{\theta} \\ \chi_E &= -\bar{\mathbf{u}} \cdot \nabla \bar{\eta} - \nu \Delta \bar{\eta} + \bar{\mathbf{w}} \cdot \hat{\mathbf{g}} \beta \end{aligned} \quad (57)$$

The derivation of the weak form with embedded turbulence model in Eq. (56) is based on hierarchical decomposition as shown in Fig. 2. Subsequently, the development of the closure model is based on variational embedding as shown in Fig. 4. The algorithmic form of the proposed residual-based turbulence model for density-stratified incompressible flows is presented in Algorithm 1.

5. Numerical tests

The performance of the proposed turbulence model for stratified turbulent flows is evaluated on canonical test cases for which an extensive database of published DNS and LES results is available for quantitative comparison. These include the well-known thermal instabilities, namely, the Rayleigh–Bénard instability and the Rayleigh–Taylor instability. Also presented is the case of stratified plane turbulent flow. These problem classes cover a range of physics of flows and account for various combinations of the boundary conditions.

Algorithm 1: The proposed residual-based turbulence model in the algorithmic form within one time-step.

input : $\mathbf{u}^n, p^n, \theta^n, (\mathbf{u},t)^n, (\theta,t)^n$ from time-step n

- 1 Start the loop of time-step $n + 1$;
- 2 Initialize the iteration counter: $i \leftarrow 0$;
- 3 Predictors: $\mathbf{u}_i^{n+1} = \mathbf{u}^n; p_i^{n+1} = p^n; \theta_i^{n+1} = \theta^n; (\mathbf{u},t)_i^{n+1} = \frac{\gamma-1}{\gamma}(\mathbf{u},t)^n; (\theta,t)_i^{n+1} = \frac{\gamma-1}{\gamma}(\theta,t)^n$;
- 4 Compute the initial residual $R_0 = \|\mathbf{R}_i^{n+1}\|_2$ following Eq. (22);
- 5 **while** $\|\mathbf{R}_i^{n+1}\|_2 \geq \text{tol} \cdot R_0$ **do**
- 6 Compute the stability tensor $\boldsymbol{\tau}_i^{n+1}$ for the fine-scale level-I by solving Eq. (42);
- 7 Compute the stability tensor $\boldsymbol{\tau}_i^{n+1}$ for the coarse-scale by solving Eq. (54);
- 8 Following Eq. (22), compute the consistent tangent \mathbf{K}_i^{n+1} and the residual \mathbf{R}_i^{n+1} to form the algebraic system $\mathbf{K}_i^{n+1}[\Delta\mathbf{u}_i^{n+1}, \Delta p_i^{n+1}, \Delta\theta_i^{n+1}]^T = \mathbf{R}_i^{n+1}$;
- 9 Solve the linearized system;
- 10 Update solution fields: $\mathbf{u}_{i+1}^{n+1} = \mathbf{u}_i^{n+1} + \Delta\mathbf{u}_i^{n+1}; p_{i+1}^{n+1} = p_i^{n+1} + \Delta p_i^{n+1}; \theta_{i+1}^{n+1} = \theta_i^{n+1} + \Delta\theta_i^{n+1}$;
- 11 Update transient fields: $(\mathbf{u},t)_{i+1}^{n+1} = (\mathbf{u},t)_i^{n+1} + \frac{1}{\gamma\Delta t}\Delta\mathbf{u}_i^{n+1}; (\theta,t)_{i+1}^{n+1} = (\theta,t)_i^{n+1} + \frac{1}{\gamma\Delta t}(\Delta\theta_i)^{n+1}$;
- 12 Update the iterator: $i \leftarrow i + 1$;
- 13 **end**

output: $\mathbf{u}^{n+1}, p^{n+1}, \theta^{n+1}, (\mathbf{u},t)^{n+1}, (\theta,t)^{n+1}$ of current time-step $n + 1$

5.1. Code development and solution procedure

The proposed turbulence model is implemented in an in-house finite-element program. The parallel version for distributed-memory computing is based on the message-passing interface (MPI) that is enabled via the open-source package PETSc [54]. Variational consistency of the model results in quadratic convergence in the nonlinear solution loop within each time-step of the generalized- α method. The tolerance criterion for the relative L_2 norm of the initial residual is set as 10^{-6} . We employ the generalized minimal residual algorithm (GMRES) together with the block Jacobi preconditioner to solve the discretized linearized system in each iteration within the Newton–Raphson loop. The relative and the absolute tolerances for the iterative solver are both set as 10^{-12} . The algorithmic form of the solution procedure employing the proposed residual-based turbulence model is presented in Algorithm 1. To help the interested reader in the implementation of the method, detailed expressions of the linear systems at the different levels of variational formulations are presented in the [Appendices](#).

Lines 6 and 7 in Algorithm 1 show that coarse-scale and fine-scale stability tensors are locally and dynamically updated within each iteration of the Newton–Raphson loop in the time marching of the nonlinear weak form. These two steps introduce additional computational cost as compared to the conventional stabilized method, and this aspect is discussed in [Appendix B](#). However, it is important to note that these variationally derived stability tensors preclude the need for any user-defined or user-designed tunable parameters to be introduced in the model.

5.2. Rayleigh–Bénard convection

In this section we carry out a series of numerical studies of the classic Rayleigh–Bénard convection problem to validate the accuracy of the proposed method. Both two-dimensional (2D) and three-dimensional (3D) cases are considered, where an applied background temperature gradient drives the flow. This problem is of relevance in natural and engineered flows [55]. Two governing parameters in this class of problems are the Rayleigh number Ra , and the Prandtl number Pr . We can write the kinematic viscosity ν and thermal diffusivity α in terms of Ra and Pr as follows:

$$\nu = \sqrt{\frac{Pr}{Ra}} \quad \text{and} \quad \alpha = \sqrt{\frac{1}{Pr Ra}} \tag{58}$$

All test cases in this section are assigned a unit buoyancy force (i.e., $\beta|\hat{\mathbf{g}}| = 1$), the direction of which is case-specific.

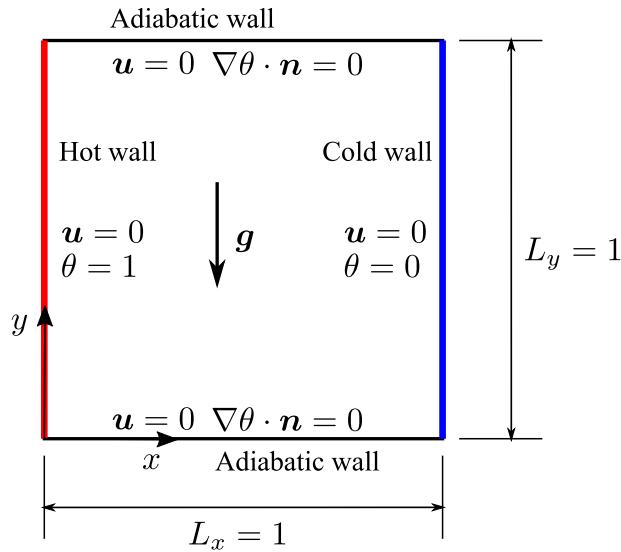


Fig. 5. Schematic diagram of the 2D Rayleigh–Bénard problem: hot wall (red), cold wall (blue) and adiabatic walls (black). (For interpretation of the references to color in this figure legend, the reader is referred to the web version of this article.)

5.2.1. Natural convection in 2D cavity enclosure

When the gravitational force is approximately perpendicular to the temperature gradient it is termed as natural convection. The first test case is a 2D thermally driven flow where the left and right walls have applied temperature boundary condition to provide a constant background temperature gradient as the driving mechanism for the problem. The top and bottom surfaces are both adiabatic walls. In the fluid phase, all four walls are applied with no-slip and no-penetration conditions, and a zero-pressure reference point is set at the bottom left corner to eliminate the constant pressure mode. The computational domain is a bi-unit box (i.e., $[0, 1] \times [0, 1]$) and the schematic diagram of problem description and boundary conditions is presented in Fig. 5. The unit gravity force is applied in the negative y -direction, and the thermal expansion coefficient is set as $\beta = 1$. The Prandtl number Pr is set equal to 0.71 that represents the physics of air flow. Although the exact solution for natural convection is presented in Chenoweth and Paulucci [56] for cases with $Ra \rightarrow 0$, flows of interest in engineering analysis occur at much higher Rayleigh numbers (i.e., $Ra > 10^6$) for which analytical solutions do not exist. Therefore, validation of the proposed method is carried out via comparison with reported numerical data, including maxima of velocity components and their locations, and with averaged Nusselt numbers when possible. The averaged Nusselt number \overline{Nu} is defined on the boundary as follows,

$$\overline{Nu} = \frac{1}{A} \int_{\Gamma} \nabla\theta \cdot \mathbf{n} \, d\Gamma = \frac{1}{A} \sum_{e=1}^{N_{seg}} \int_{\Gamma^e} \nabla\theta \cdot \mathbf{n} \, d\Gamma \tag{59}$$

where A is the area of the wall and N_{seg} is the number of segments on the wall in the current mesh. In other words, the averaged Nusselt number \overline{Nu} represents the total heat flux at the boundary. Four different Rayleigh numbers are selected (i.e., 10^7 , 10^8 , 10^9 and 10^{10}) to cover the span of the transitional (10^7 and 10^8) and turbulent (10^9 and 10^{10}) natural convections [39,55,57].

We first carried out a mesh dependency study with the proposed method to identify an appropriate mesh for the given Ra to be used in the quantitative comparison with the reported numerical results in the literature. All four test cases for the selected Ra were started with a mesh comprised of 25×25 bilinear quadrilateral (Q4) elements. We refined the mesh by doubling the number of elements in both the dimensions till the difference of averaged Nusselt numbers at the hot wall between two successive meshes was smaller than 0.001. All meshes were stretched in both horizontal and vertical directions by Chebyshev grid to have enough mesh resolution for the fluid and thermal boundary layers. The post-processed averaged Nusselt numbers at the hot wall for the different Ra and mesh resolutions are listed in Table 1. The snapshots of the instantaneous relative temperature field and the velocity

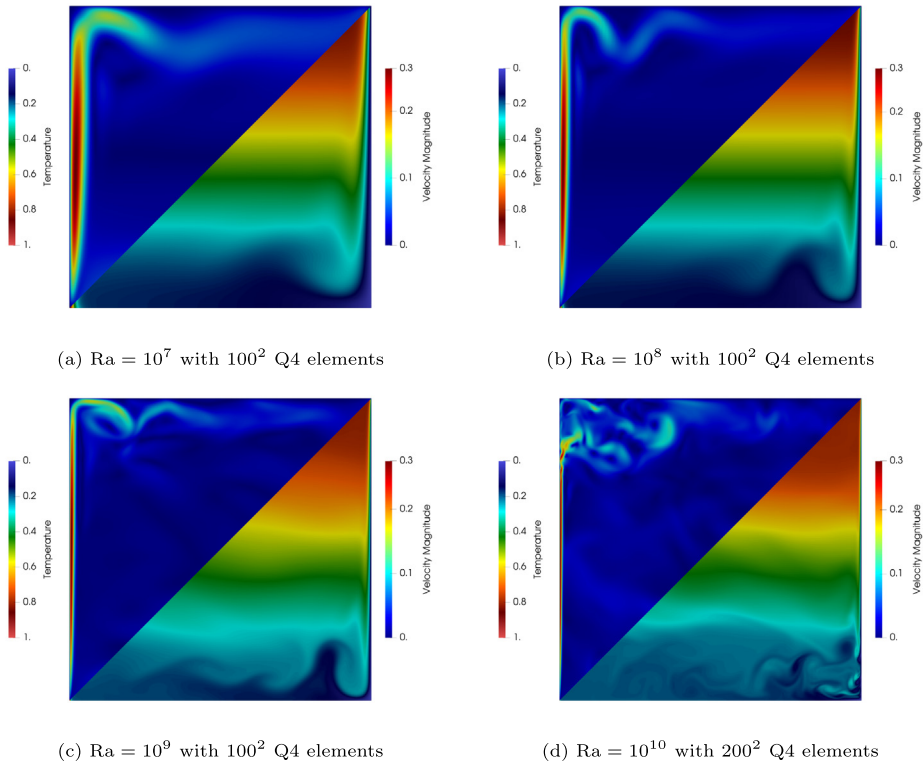


Fig. 6. Instantaneous velocity and temperature fields of natural convection in a 2D enclosure with varying Ra number.

Table 1

Averaged Nusselt number \overline{Nu}_h at the hot wall for different Ra : mesh dependency study.

Ra	10^7	10^8	10^9	10^{10}
25×25	16.6482	30.1542	53.5766	98.9238
50×50	16.5334	30.2440	54.4188	97.7409
100×100	16.5196	30.2400	54.4325	97.4803
200×200	—	—	—	97.4747

field for the four Ra cases with their corresponding refined meshes are presented in Fig. 6. While the two cases in the transitional regime gradually approach a steady state as shown in Figs. 6(a) and 6(b), the solution fields in the two turbulent cases are only statistically quiescent. As shown in Figs. 6(c) and 6(d), the velocity and temperature fields from the turbulent cases exhibit unsteady flow structures near the top-left and the bottom-right corners, where the flow convection which is accelerated by thermal buoyancy competes with the viscous dissipation effects. In the quantitative comparison study of the statistically stationary quantities, the solution fields from the simulation of $Ra = 10^9$ and $Ra = 10^{10}$ are averaged over 200 sample points along the time axis that are taken from 2000 steps at interval of 10 steps once the statistical steady state has reached.

We now present a quantitative comparison of the proposed residual-based turbulence model with some representative data reported in the literature that come from a range of existing computational methods for turbulent natural convection. These include DNS with pseudo-spectral method (PSM) [58], finite-volume method (FVM) with $k-\epsilon$ RANS turbulence model [59], large eddy lattice Boltzmann method (LBM) [57], and VMS method with isothermal LES turbulence model [39]. As shown in Table 2, the computed \overline{Nu}_h via the proposed turbulence model is very close to the value reported in the literature for different numerical methods and turbulence models. Another set of quantitative comparisons includes the magnitude of the maximum horizontal velocity along the vertical mid-plane (i.e., $x = 0.5$) and the magnitude of the vertical component of velocity along the horizontal mid-plane (i.e., $y = 0.5$).

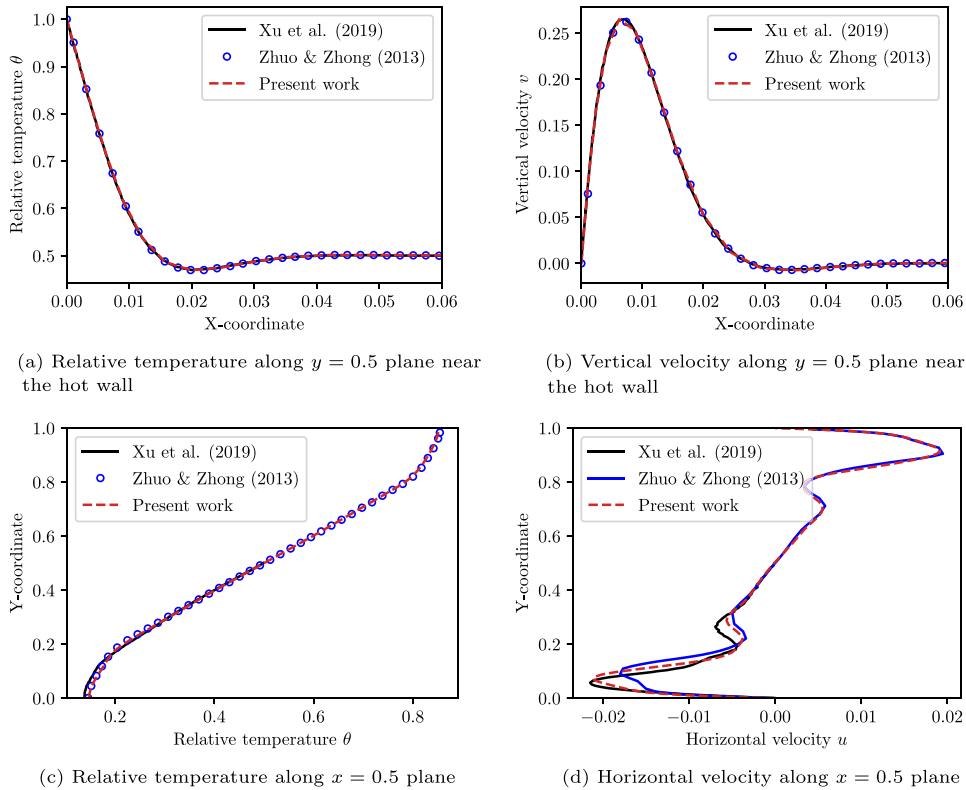


Fig. 7. Distribution of solution fields along mid-planes (i.e., $x = 0.5$ and $y = 0.5$) with $Ra = 10^9$.

Table 2

Averaged Nusselt number \overline{Nu}_h at the hot wall for different Ra : validation study.

Ra	10^7	10^8	10^9	10^{10}
FVM [59]	–	30.1	54.4	97.6
LBM [57]	16.512	30.195	54.510	98.171
VMS (Isothermal) [39]	16.44	30.1	54.29	97.29
Present work	16.5196	30.2400	54.4325	97.4747

The statistically processed results from the transitional and turbulent flow regimes are compared with the reference data in Tables 3 and 4, respectively. The location and magnitude of the maxima of velocity components validate the accuracy of the proposed method. To further verify our numerical results, we present the distribution of the solution fields (i.e., u , v and θ) along certain critical planes (i.e., $x = 0.5$ and $y = 0.5$). Fig. 7 shows spatial distribution of statistically averaged fields for $Ra = 10^9$ and a good agreement with the reference data [39,57] is observed. The distribution of u in the bottom half of the mid-plane shows some deviation in Fig. 7(d), where our results are closer to the data reported in [39] near the bottom wall and match with [57] away from the wall. Similarly, spatial distributions of solution fields for $Ra = 10^{10}$ along the mid-planes are plotted in Fig. 8, where a good agreement between our simulations and other published numerical results is achieved.

5.2.2. Natural convection in 3D cavity enclosure

In this section, we extend the 2D natural convection discussed in Section 5.2.1 to 3D, where the walls normal to the z -axis are insulated and imposed with no-slip boundary conditions, as shown in Fig. 9. To make the geometry of the computational domain consistent with the experimental setup [60], the dimension of z -axis is set equal to 0.32. The vector of acceleration due to gravity is pointed in the negative y -direction (i.e., $\hat{g} = [0, -1, 0]$). The Rayleigh number is set equal to $Ra = 1.5 \times 10^9$, which makes the flow physics lie in the turbulent regime. Due

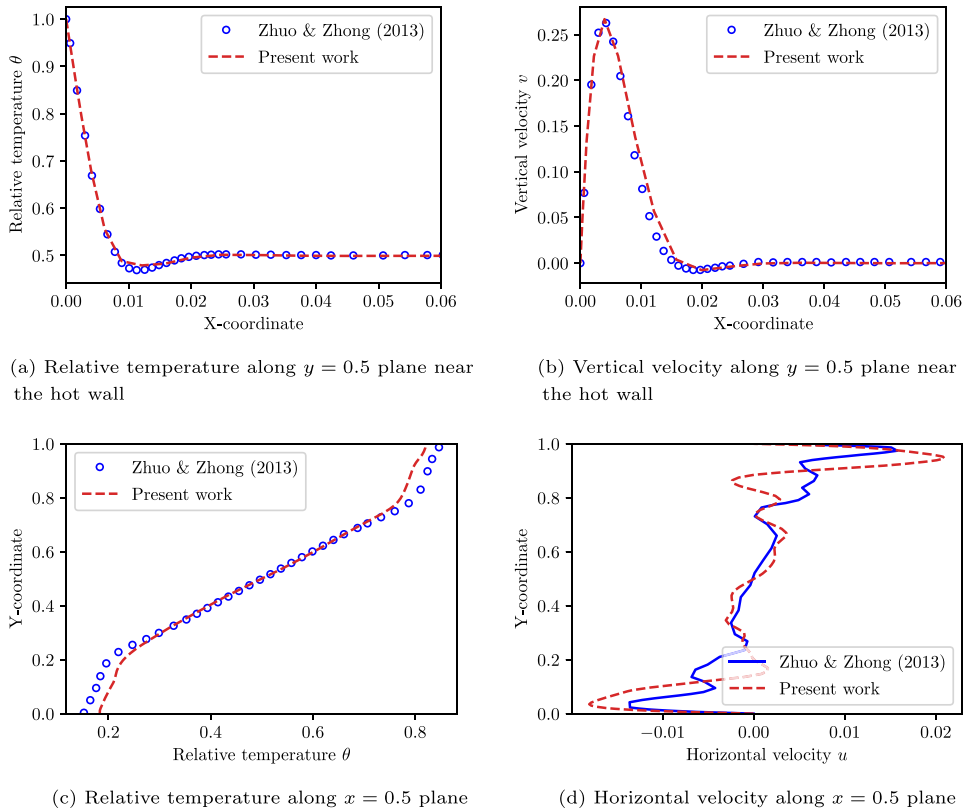


Fig. 8. Distribution of solution fields along mid-planes (i.e., $x = 0.5$ and $y = 0.5$) with $Ra = 10^{10}$.

Table 3

Values and locations of velocity maxima of 2D natural convection in the transitional regime.

Ra	10^7				10^8			
	u_{\max}	y	v_{\max}	x	u_{\max}	y	v_{\max}	x
PSM [58]	0.0562	0.879	0.270	0.021	0.0385	0.928	0.266	0.012
FVM [59]	—	—	—	—	0.0615	0.941	0.217	0.0135
LBM [57]	0.05635	0.8779	0.2626	0.0217	0.03846	0.9209	0.264	0.125
VMS (Isothermal) [39]	0.0564	0.878	0.264	0.023	0.0399	0.930	0.266	0.0125
Present work	0.0558	0.8852	0.2622	0.0199	0.03703	0.9222	0.2648	0.0120

Table 4

Values and locations of velocity maxima of 2D natural convection in the turbulent regime.

Ra	10^9				10^{10}			
	u_{\max}	y	v_{\max}	x	u_{\max}	y	v_{\max}	x
FVM [59]	—	—	—	—	0.0278	0.9625	0.202	0.0055
LBM [57]	0.01987	0.9134	0.2645	0.00731	0.01627	0.9791	0.2650	0.00417
VMS (Isothermal) [39]	0.0270	0.931	0.267	0.00667	0.0143	0.956	0.270	0.00375
Present work	0.02110	0.9304	0.2653	0.006153	0.02095	0.9455	0.2678	0.003942

to the thermal and flow boundary layers along the walls in all the three dimensions, a tensor-product Chebyshev grid $\mathbf{C}_{x_n} = C_{x_n} \times C_{y_n} \times C_{z_n}$ is developed, where $\mathbf{x}_n = [x_n, y_n, z_n]^T$ are the number of nodes in each dimension, respectively. Two meshes of trilinear hexahedral elements (H8) including a coarse mesh (i.e., $\mathbf{x}_n = [51, 51, 17]^T$) and a fine mesh (i.e., $\mathbf{x}_n = [101, 101, 33]^T$) are used in the numerical tests in this subsection. To highlight the

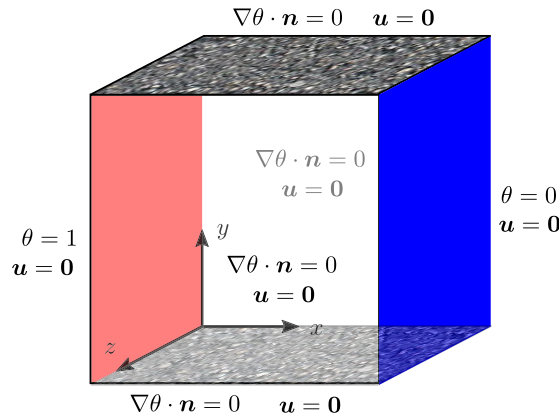


Fig. 9. Schematic diagram of 3D natural convection: the hot wall (red), the cold wall (blue) and adiabatic walls (shaded). (For interpretation of the references to color in this figure legend, the reader is referred to the web version of this article.)

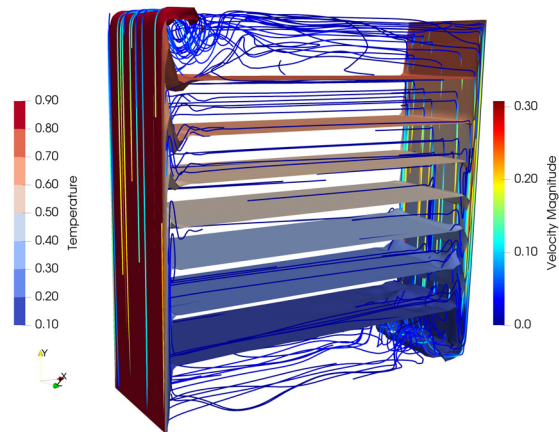


Fig. 10. Natural convection in a 3D enclosure: isocontours of relative temperature θ and streamlines of velocity field \mathbf{u} colored by its magnitude. (For interpretation of the references to color in this figure legend, the reader is referred to the web version of this article.)

higher spatial accuracy of our method as compared to the published literature, we compute our results on the mesh with $\mathbf{x}_n = [101, 101, 33]^T$ which corresponds to the coarsest mesh employed in [39,57,60], and compare our computed results with the data from the finest mesh employed in these references. We also employ a still lower resolution mesh to showcase the fine-scale modeling feature of our method that automatically compensates for the crudeness of spatial discretization and results in the higher spatial accuracy of the solution. To visualize the flow field, the streamlines of velocity and iso-surfaces of temperature are plotted in Fig. 10. Once the simulation reaches the statistical steady state, we carry out time-averaging of the solution fields. In Fig. 11, the time-averaged results are compared with the reported numerical results, including DNS [60] and LES [39,57]. Fig. 11 presents spatial distribution of the relative temperature and vertical component of the velocity near the hot wall along a plane at $y = 0.5$. A good agreement with published DNS and LES data obtained from various numerical methods and turbulence models is attained.

The proposed method has also been implemented with linear (T4) and quadratic tetrahedral (T10) elements. Accordingly, we rearrange the element connectivity for the finer mesh (i.e., $\mathbf{x}_n = [101, 101, 32]^T$) to accommodate the linear tetrahedral (T4) and quadratic tetrahedral (T10) elements while maintaining the number and location of nodes similar to that in hexahedral element meshes. The computed results with the different members of the family of 3D Lagrange elements are presented in Fig. 12. The solution fields obtained from simulations with different types

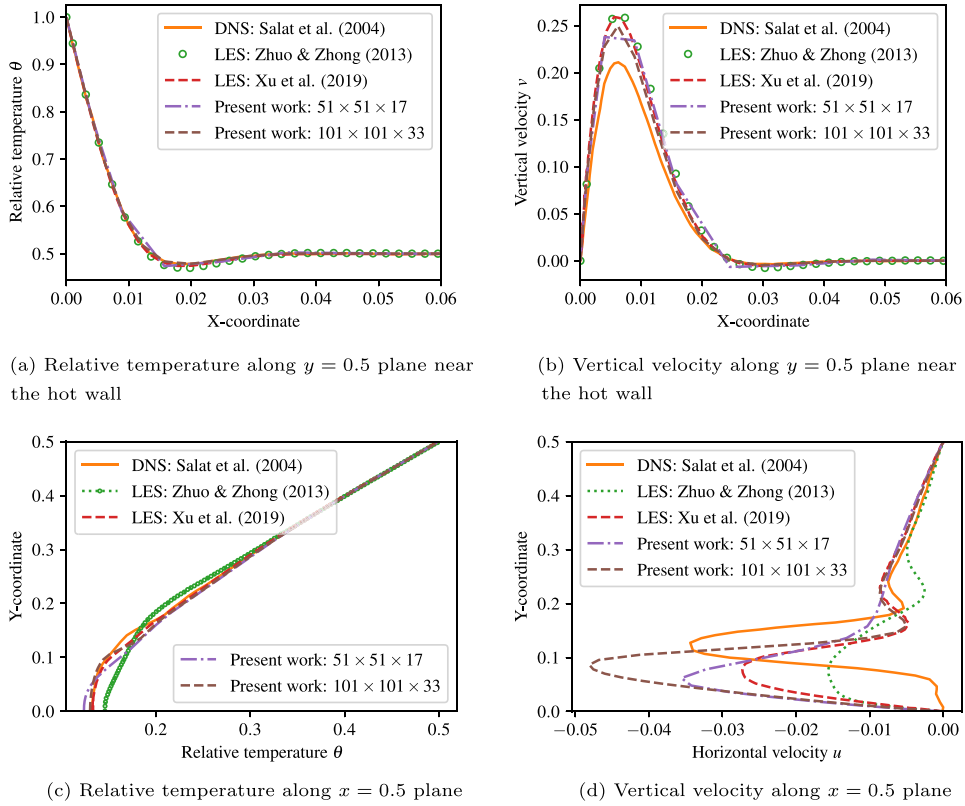


Fig. 11. Natural convection in 3D enclosure ($Ra = 1.5 \times 10^9$): validation study.

of elements and for different orders of polynomials are almost identical (Figs. 12(a)–12(c)), while the distribution of horizontal velocity shows some variation between the different element types, as presented in Fig. 12(d).

5.2.3. 3D Rayleigh–Bénard instability

This section investigates the well-known Rayleigh–Bénard convection, where gravity acts in the opposite direction to the temperature gradient. The schematic diagram of the problem is presented in Fig. 13. In this problem, the buoyancy generated by the stratification is counteracted by the viscous damping effect, and the ratio of these two effects defines the Rayleigh number. Once the Rayleigh number reaches a certain level, the Rayleigh–Bénard instability gets triggered and drives the flow physics. The computational domain is a unit cubic, which is discretized into 64^3 H8 elements. Slip boundary conditions are applied at the top and bottom surfaces (i.e., $z = 0$ and $z = 1$), while periodic boundary conditions for all the fields are applied at the walls perpendicular to the x - and y -directions. The grid spacing in the horizontal planes is uniform while the mesh is stretched in z -direction to adapt for the thermal boundary layer. The Rayleigh number is $Ra = 10^8$ and Prandtl number is $Pr = 1$.

We initialize the problem with a static flow and with zero-gradient temperature field. We first compare the temporal evolution of the total kinetic energy E_u , the total entropy $E_{\hat{\theta}}$ and the total Nusselt number Nu_V with the DNS (512^3) and LES (128^3) results reported in [23], as shown in Fig. 14. The expressions of the total kinetic energy E_u , total entropy $E_{\hat{\theta}}$ and total Nusselt number Nu_V for a FEM-discretized domain are given as follows:

$$E_u(t) = \frac{1}{2} \int_{\Omega} |\mathbf{u}(\mathbf{x}, t)|^2 d\Omega = \frac{1}{2} \sum_{e=1}^{nel} \int_{\Omega^e} |\mathbf{u}(\mathbf{x}, t)|^2 d\Omega \quad (60)$$

$$E_{\hat{\theta}}(t) = \frac{1}{2} \int_{\Omega} (\hat{\theta}(\mathbf{x}, t))^2 d\Omega = \frac{1}{2} \sum_{e=1}^{nel} \int_{\Omega^e} (\hat{\theta}(\mathbf{x}, t))^2 d\Omega \quad (61)$$

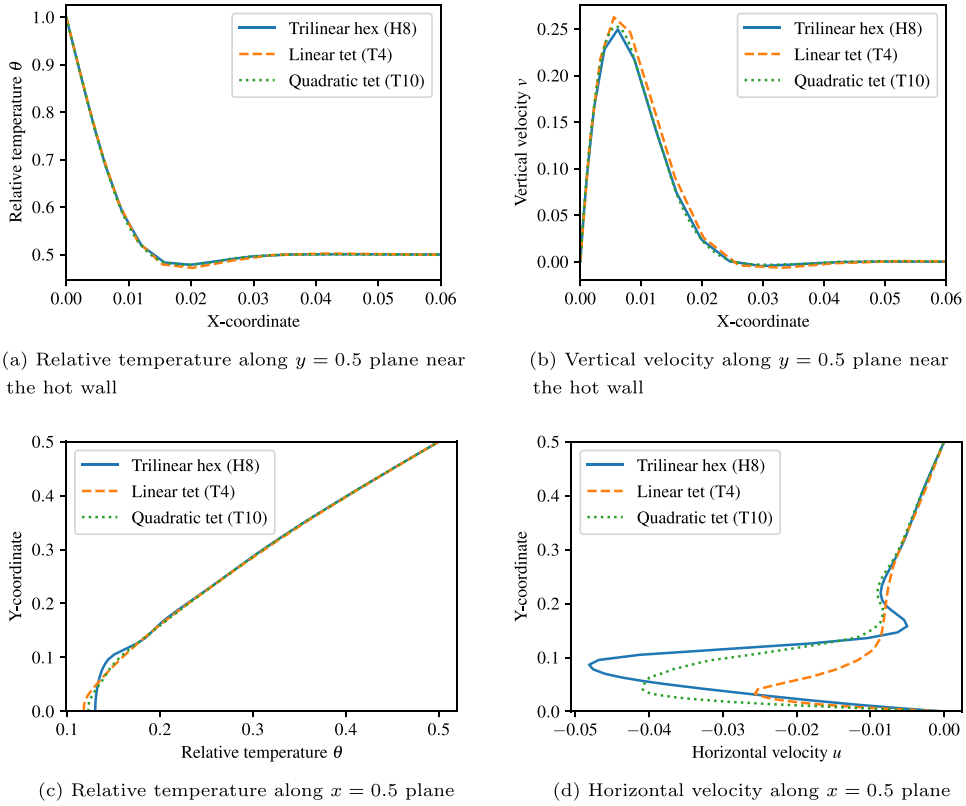


Fig. 12. Natural convection in a 3D enclosure ($Ra = 1.5 \times 10^9$): various types of elements and p -refinement study.

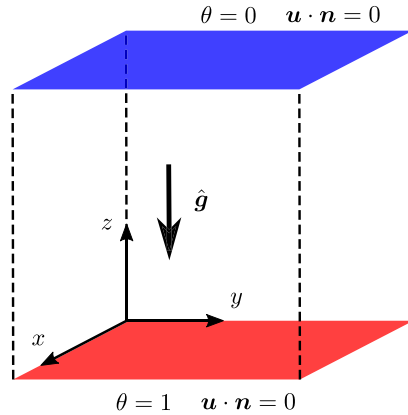


Fig. 13. Schematic diagram of the 3D Rayleigh–Bénard instability: hot wall at $z = 0$ (red) and cold wall at $z = 1$ (blue). (For interpretation of the references to color in this figure legend, the reader is referred to the web version of this article.)

$$Nu_V(t) = 1 + \frac{L_z}{\kappa \Delta\theta} \frac{1}{V} \sum_{e=1}^{nel} \int_{\Omega^e} w(\mathbf{x}, t) \hat{\theta}(\mathbf{x}, t) d\Omega \tag{62}$$

where $\hat{\theta}$ is the variation of temperature, which is calculated by subtracting the temperature due to background thermal gradient from the relative temperature θ , i.e., $\hat{\theta} = \theta - (\Delta T/L_z)z$; ΔT is the temperature difference between top and bottom planes; and V is the volume of the computational domain. Due to the different initialization strategies adopted in the various numerical techniques reported in the literature, there is difference in the early time history of



Fig. 14. Evolution of global quantities in the Rayleigh-Bénard instability.

Table 5

Time-averaged total kinetic energy E_u , total entropy $E_{\hat{\theta}}$ and total Nusselt number Nu_V : mean and standard deviation (data collected from 30 to 80).

	Mesh res.	E_u	$E_{\hat{\theta}}$	Nu_V
DNS [23]	512^3	$(2.20 \pm 0.33) \times 10^{-2}$	$(3.75 \pm 0.26) \times 10^{-2}$	55.5 ± 10.7
LES-RNG [23]	128^3	$(2.51 \pm 0.31) \times 10^{-2}$	$(3.64 \pm 0.23) \times 10^{-2}$	72.4 ± 10.9
LES-VMS	64^3	$(2.168 \pm 0.296) \times 10^{-2}$	$(3.609 \pm 0.238) \times 10^{-2}$	55.40 ± 10.67
LES-VMS	96^3	$(2.332 \pm 0.265) \times 10^{-2}$	$(3.728 \pm 0.174) \times 10^{-2}$	57.08 ± 7.32

the total kinetic energy, entropy, and Nusselt number between our simulation and the reference data [23] as shown in Figs. 14(a)–14(c). After approximately 20 flow overturning cycles, the flow reaches statistically steady state [23], and we observe a consistent and comparable trend in the time histories of total entropy, energy and Nusselt number when compared with the reference data. In Fig. 15 we present the instantaneous snapshots of the temperature field θ for two time points, one from the initial developmental stage and the other from the statistically steady state. In Fig. 15(a), when the flow begins to develop from the initial conditions, typical salt-finger flow structures develop at the top and bottom walls. At a later stage, when the flow is fully developed, a more intricate mixing pattern emerges, as is shown in Fig. 15(b).

To make quantitative comparison of the overall metrics of the turbulent thermal flow, we list the time-averaged mean and standard deviation of E_u , $E_{\hat{\theta}}$ and Nu_V from our model for two meshes (64^3 and 96^3 trilinear hexahedrons) with the published DNS and LES results [23] in Table 5. The time averaging is carried out over the range from 30 to 80 dimensionless time units. Finally, we compare the vertical distribution of the space-time averaged (x - y plane and time t) mean and fluctuation rms of temperature in Figs. 16(a) and 16(c) and vertical velocity in Figs. 16(b) and 16(d) with the reported DNS and LES results [23], respectively. The rms profile of vertical velocity (Fig. 16(b)) from our simulation closely matches the reference DNS and LES results [23], while the mean profile of temperature field

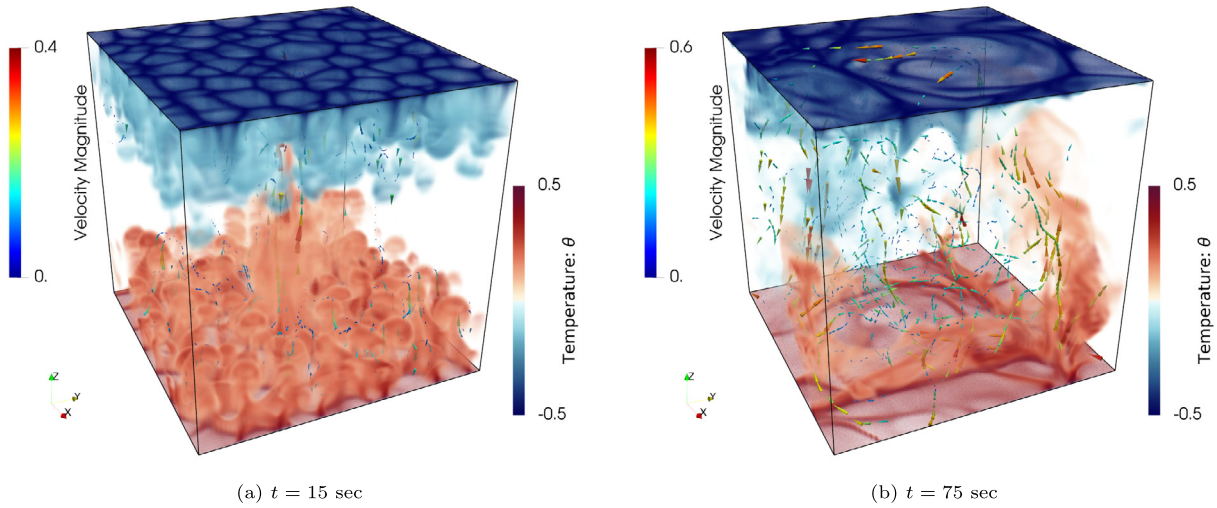


Fig. 15. Relative temperature field (volume rendered) and streamlines of velocity (cones colored by its magnitude) in Rayleigh–Bénard Instability: initial development and statistically stationary stages. (For interpretation of the references to color in this figure legend, the reader is referred to the web version of this article.)

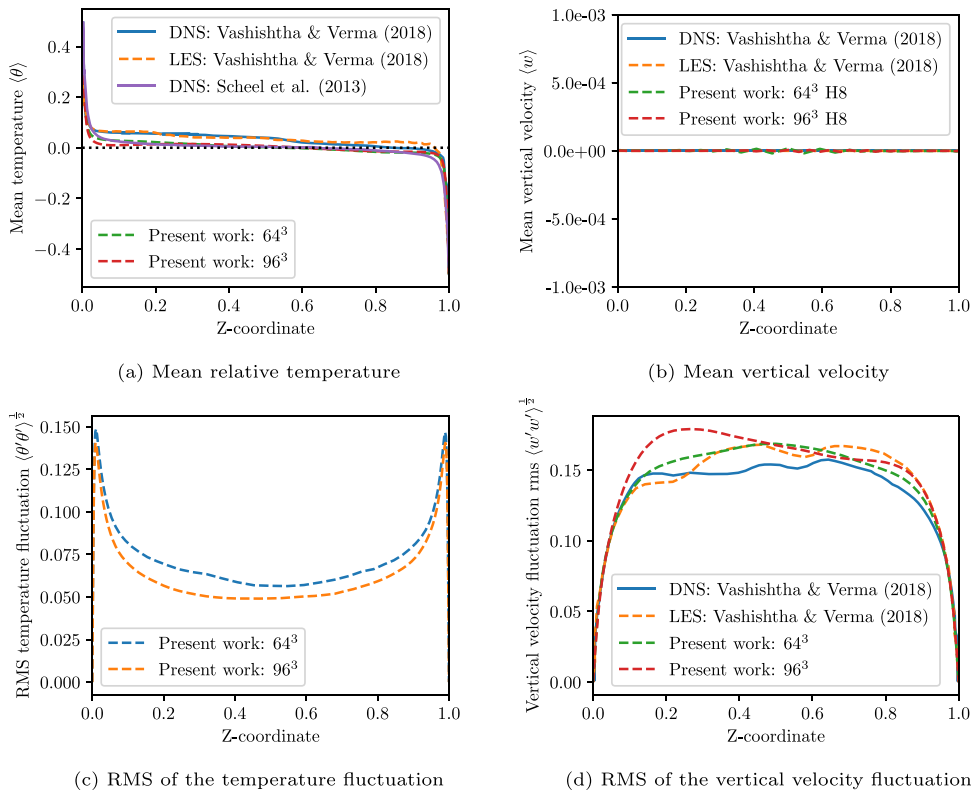


Fig. 16. Vertical profiles of flow statistics for the Rayleigh–Bénard instability.

(Fig. 16(a)) slightly deviates from the profiles reported in [23]. We have also added to Fig. 16(a) the mean profile for a closed domain Rayleigh–Bénard Instability [61] with the same Ra and similar Pr , which shows a symmetric

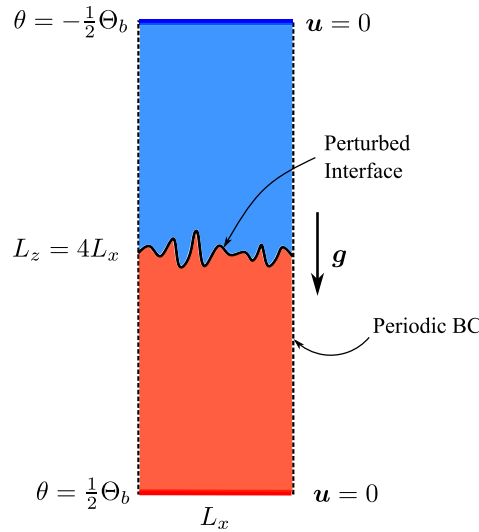


Fig. 17. Schematic diagram of the 2D Rayleigh–Taylor instability: the hot fluid (red region), the cold fluid (blue region) and the perturbed interface (black). (For interpretation of the references to color in this figure legend, the reader is referred to the web version of this article.)

distribution of the mean temperature that coincides with our results. Fig. 16(b) presents the profile of the vertical velocity in the wall normal distribution, computed with the coarse mesh, which shows small variations around zero at a scale of 10^{-5} , while the reference numerical results show variation that lies within a range of 10^{-13} . This is attributed to the use of much lower order of polynomials (H8) as compared to the global interpolation functions employed in the pseudo-spectral method presented in [23]. In general, our simulations show superior statistical results for the 3D Rayleigh–Bénard instability problem as compared to the LES method that employs turbulent viscosity type model.

5.3. 2D Rayleigh–Taylor instability in miscible flows

In this section we evaluate the performance of the proposed LES method via the simulation of turbulent mixing layers [62], that are driven by the well-known Rayleigh–Taylor instability (RTI) [63]. The physical mechanism of RTI is that the gravitational force acting on the fluid is opposed by its density gradient, which eventually leads to large scale turbulent mixing. RTI plays an important role in various natural phenomena, ranging from the cirrus clouds in the sky [64] to the nebulae resulting from the residual of a supernova [65]. This phenomenon also appears in engineered flows where RTI and other hydrodynamic instabilities affect the efficiency of energy harvesting devices in inertial confinement fusion (ICF) [66].

The problem description is presented in Fig. 17. No penetration and no slip conditions are applied to the velocity field at the top and bottom boundaries. The relative temperature field is also specified at the top and bottom surfaces as presented in Fig. 17. Periodic boundary conditions are applied along the left and right boundaries. The aspect ratio of the domain is $L_y/L_x = 4$. The computational domain is discretized into 256×1024 uniform linear quadrilateral (Q4) elements, while the reference DNS simulation [67] uses 2048×8196 grid points. We select the multi-mode initial condition [66] to accelerate the development of turbulent mixing by applying a high-frequency perturbation to the initial interface between the hot/cold fluids (or the light/dense fluids). The expression for the initial temperature field θ_0 with a perturbed interface, as suggested in Clark [68], is as follows.

$$Y_s(x) = \frac{1}{2} \left(1 + \frac{1}{N_y} \sum_{k=30}^{60} \cos(2\pi x + \phi_k) \right) \tag{63}$$

$$\theta_0(x, y) = -\frac{1}{2} \tanh(1.28N_y(y - Y_s(x))) + \frac{1}{2} \tag{64}$$

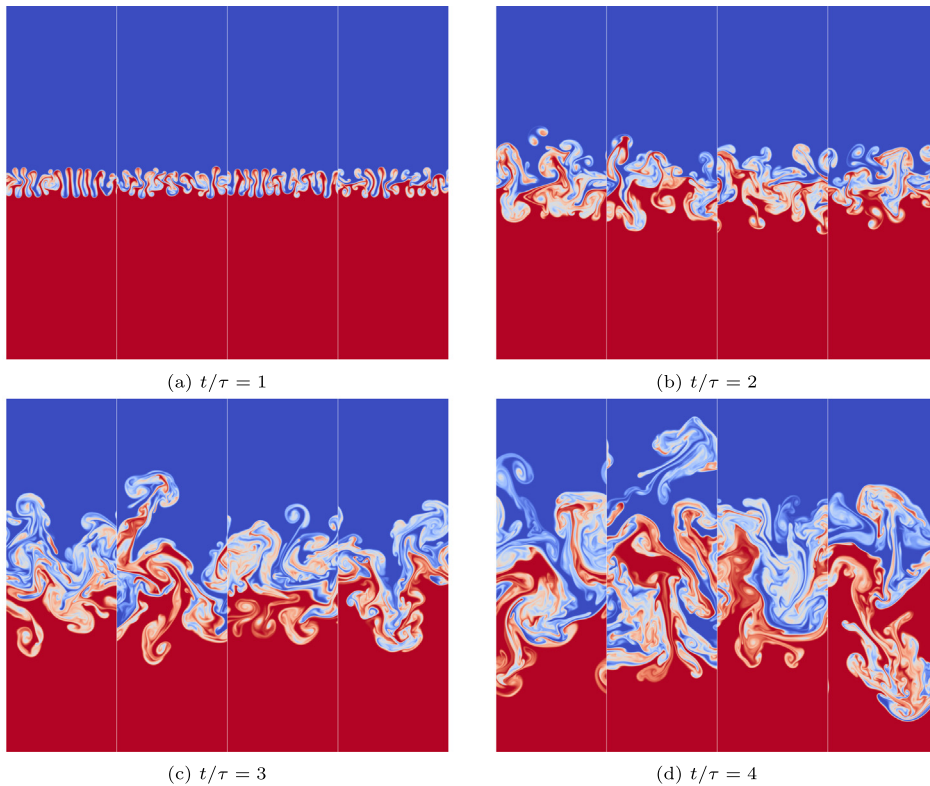


Fig. 18. Evolution of the temperature field in the Rayleigh–Taylor instability: 4 selected realizations.

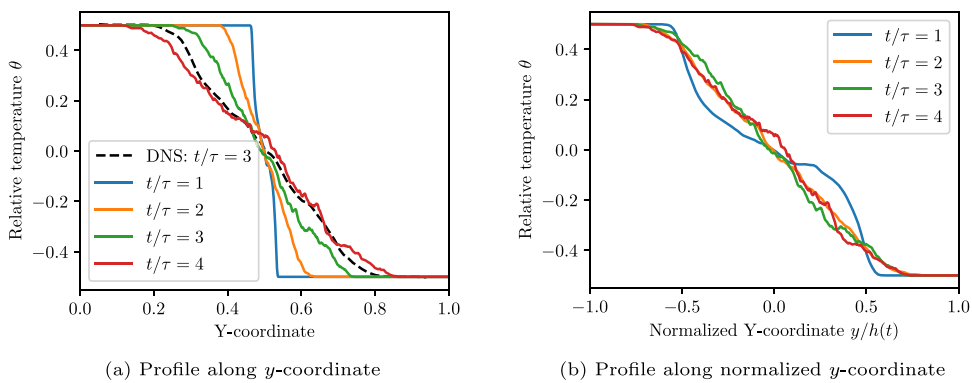
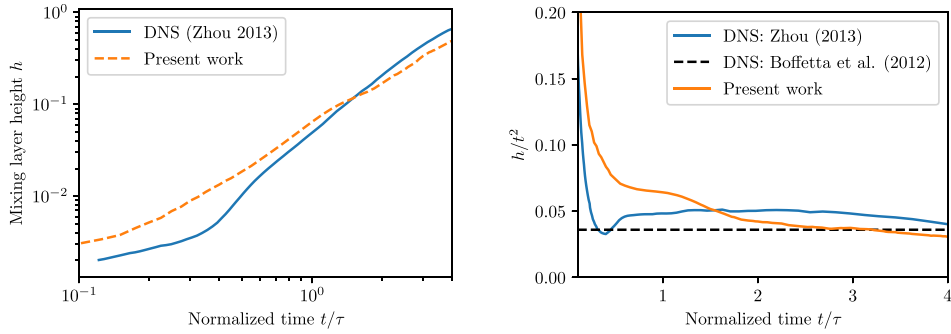


Fig. 19. Flow statistics in the Rayleigh–Taylor instability: mean profiles of the relative temperature field θ at various time points.

where ϕ_k is a uniformly distributed random phase ranging from 0 to 2π . The kinematic viscosity ν and the thermal viscosity κ are both set as $\nu = \kappa = 1.58 \times 10^{-6}$. The magnitude of gravitational acceleration vector $|\hat{g}|$ and the thermal expansion coefficient β are both 0.5. For the purpose of ensemble averaging, 25 different realizations with different random initial conditions are simulated. Four realizations are selected to visualize the evolving temperature field, as shown in Fig. 18.

The mean profile of the temperature field is generated through ensemble averaging, which is defined as follows,

$$\langle \theta \rangle (y, t) = \frac{1}{N} \sum_{n=1}^N \frac{1}{L_x} \int_0^{L_x} \theta_n(x, y, t) dx \tag{65}$$

(a) Mixing layer height h with respect to normalized time(b) Scaled Mixing layer height h/t^2 with respect to normalized time**Fig. 20.** Time history of mixing layer height h : indication of the quadratic law $h(t) \propto t^2$.

where n denotes the counter for the number of cases in a total of $N = 25$ realizations. To quantitatively analyze the results, we first plot the ensemble-averaged temperature field at 4 different time points in Fig. 19(a). A comparison with the DNS temperature profile at $t/\tau = 3$ reveals that as the flow develops, it triggers turbulent mixing and the present simulations match well with the DNS data. Next, we normalize the vertical coordinates with the thickness of mixing layer $h(t)$ where temperature has dropped to 40% of the prescribed boundary temperature, which is defined as

$$\langle \theta \rangle \left(y = \pm \frac{1}{2} h \right) = \mp 0.4 \Theta_b \quad (66)$$

The distribution of the temperature field along the normalized vertical coordinates at various time points is presented in Fig. 19(b). The curves in Fig. 19(b) at $t/\tau = 2, 3, 4$ are almost identical which suggests that the flow is self-similar with respect to time. However, the temperature distribution at $t/\tau = 1$ deviates from others, which supports the argument for the slower development of turbulent mixing. The time history of mixing layer thickness h is presented on log scale with the DNS results [67] in Fig. 20(a). Also, the time history of scaled mixing layer thickness h/t^2 is presented in Fig. 20(b), where a plateau is observed after 1.5 units of normalized time. This plateau stage suggests that the coefficient between the scaling law of h and t^2 is a constant when turbulent mixing is fully developed, and this is consistent with the reported data [67,69] as shown in Fig. 20(b). To further identify the self-similarity state predicted by our turbulence model, we plot the ratio between the rms value of the horizontal and vertical velocity components (i.e., $\langle u'u' \rangle_{\text{mix}}^{\frac{1}{2}}$ and $\langle v'v' \rangle_{\text{mix}}^{\frac{1}{2}}$) in the mixing zone with respect to the normalized time in Fig. 21. The evolution of the ratio between the rms values of both velocity components illustrates a plateau stage after 2 dimensionless time units, which is consistent with the self-similar stage identified in Fig. 20(b). The ratio is around $\langle u'u' \rangle_{\text{mix}}^{\frac{1}{2}} / \langle v'v' \rangle_{\text{mix}}^{\frac{1}{2}} = 1.2$ in the self-similar stage, which matches with the published data in [67]. Finally, we calculate the global Reynolds number (i.e., $Re = \sqrt{\langle u'u' \rangle_{\text{mix}} + \langle v'v' \rangle_{\text{mix}}} h / \nu$) and Rayleigh number (i.e., $Ra = \beta g \Theta_b h^3 / \nu \kappa$) of the system at every time-step and extract the scaling between these two global quantities in Fig. 22. It is worth noticing that the proposed residual-based turbulence model for stratified turbulence successfully predicts the ultimate-state scaling (i.e., $Re \propto Ra^{\frac{1}{2}}$) [2].

5.4. Stratified plane Couette flow

This test case evaluates the performance of the proposed turbulence model via plane Couette flow with stable stratification. The flow field is bounded by two parallel infinite planes with no-slip and no-penetration boundary conditions applied at top and bottom surfaces (in the wall-normal direction). The plane Couette flow is driven by a prescribed velocity field along the top and bottom planes ($u_2|_{y=\pm 1} = \pm U_w$), as shown in Fig. 23. The dimension of the computational domain shown in Fig. 23 is same as that in the published DNS [70] and LES test cases with anisotropic minimum-dissipation model (AMD) [71]. A background temperature gradient is applied in the positive y -direction of the domain via the application of Dirichlet boundary condition for the temperature field at the top

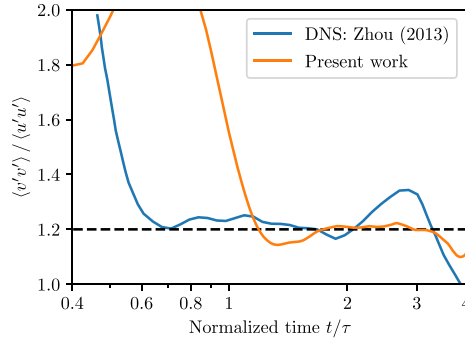


Fig. 21. The ratio between the rms value of the horizontal and vertical velocity components in the mixing zone with respect to normalized time in log scale.

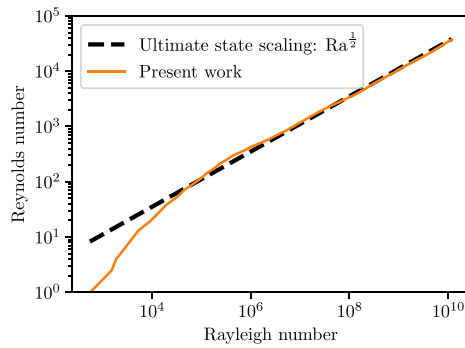


Fig. 22. Scaling between the global Re and Ra .

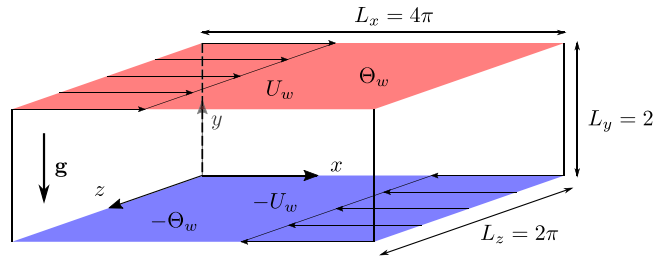


Fig. 23. Schematic diagram of the plane Couette flow with stable stratification: hot wall at $y = 2$ (red) and cold wall at $y = 0$ (blue). (For interpretation of the references to color in this figure legend, the reader is referred to the web version of this article.)

and bottom planes ($\theta|_{y=\pm 1} = \pm \Theta_w$). Both temperature and velocity fields are periodic in x - (streamwise) and z - (spanwise) directions. The unit gravitational acceleration vector (i.e., $\mathbf{g} = [0, -1, 0]$) is acting in the opposite direction to the background temperature gradient, which triggers stable stratification. A structured mesh of trilinear hexahedral (H8) elements is generated with uniform distribution of grid points in the streamwise and spanwise directions, while in the wall-normal direction, the grid is stretched to resolve the thermal boundary layer at the top and bottom surfaces. The mapping from a uniform mesh in a 1D domain $[0, 1]$ with N_y nodes to the designated stretched mesh in the wall-normal direction with the range $y \in [0, 2]$ is defined as

$$y_j^s = 1 - \frac{\tanh(C(1 - 2y_j))}{\tanh(C)} \tag{67}$$

where y_j is the coordinate of the j th node in the uniform mesh of $[0, 1]$, y_j^s is the coordinate after stretching, and C is a tunable stretch coefficient. A value of $C = 3$ has been used in each of the test cases presented below.

Table 6

Summary of the wall-resolved LES simulation of the stratified plane Couette flow with varying Pr and Ri : N_x , N_y and N_z are number of nodes in each direction; VMS: the present work, AMD: LES results with anisotropic minimum-dissipation model [71]; Re_τ and Nu , see Eq. (70).

Case	Re	Pr	Ri	$N_x(N_z)$	N_y	Re_τ			Nu		
						VMS	AMD	DNS	VMS	AMD	DNS
A1	4250	0.7	0	64	49	220.7	223	233	9.82	10.6	10.6
A2	4250	0.7	0.01	64	49	207.35	212	215	8.61	9.6	9.26
A3	4250	0.7	0.04	64	49	171.57	183	181	5.64	7.1	6.4
B1	4250	7	0	64	65	219.5	223	233	27.87	34.3	31.8
B2	4250	7	0.01	64	65	215.85	228	211	26.74	33.0	29.7
B3C	4250	7	0.04	64	65	203.52	209	206	24.21	28.1	25.9
B3F	4250	7	0.04	128	97	207.66	209	206	25.47	28.1	25.9
B4	4250	7	0.12	64	65	152.03	130	129	13.09	9.87	8.47

The governing parameters of plane Couette flows are the Reynolds number Re , Richardson number Ri and Prandtl number Pr . Accordingly, the material parameters can be written in terms of Re , Ri and Pr as follows

$$v = \frac{U_w}{Re}, \quad \beta = \frac{Ri U_w^2}{\Theta_w}, \quad \alpha = \frac{v}{Pr} = \frac{U_w}{Re Pr} \tag{68}$$

To quantitatively validate the simulations, a group of control parameters with varying Pr and Ri was selected, which is a subset of the cases considered in the reference results. The values of the parameters for these test cases are given in Table 6. The simulations were initialized with perturbed laminar Couette flow fields with constant temperature gradient. The perturbation was constructed with uniformly distributed random noise with an intensity of $0.1U_w$. As suggested by Vreugdenhil and Taylor [71], the turbulent Couette flow reaches a statistically steady state for a given set of governing parameters after a time duration of $300h/U_w$. Once the flow fields were fully developed, 500 samples were collected for a time duration of $100h/U_w$ to carry out statistical analysis. The collected flow fields were averaged in wall-normal plane as well as in the time dimension, as follows

$$\langle \bullet \rangle (y) = \frac{1}{L_x L_z T} \int_0^{L_x} \int_0^{L_y} \int_0^T \bullet(x, y, z, t) dx dz dt \tag{69}$$

For quantitative comparisons, we write the friction Reynolds number Re_τ and the Nusselt number Nu in terms of the averaged velocity and temperature gradient at the wall

$$Re_\tau = \sqrt{\frac{Re d \langle u \rangle}{U_w dy} \Big|_{y=\pm 1}}, \quad Nu = \frac{1}{\Theta_w} \frac{d \langle \theta \rangle}{dy} \Big|_{y=\pm 1} \tag{70}$$

These two parameters describe the overall flow physics in the thermal boundary layers, therefore we compare our computed Re_τ and Nu with the reported values in the literature in Fig. 24. The simulated friction Reynolds number Re_τ and the Nusselt number Nu are very close to the DNS results and the proposed model performs equally well or better as compared to the AMD-LES results that were obtained with an equal or finer mesh via the pseudo-spectral method [71]. We next examine profiles of the mean flow fields (i.e., space-time averaged streamwise velocity and temperature fields). As shown in the overlapping curves presented in Fig. 25, the proposed VMS-based turbulence model is capable of accurately modeling the stably stratified turbulent Couette flow. With increasing Richardson number, namely, stronger stable stratification, the temperature and velocity profiles in Fig. 25 becomes less steep. It is worth noticing that the mesh employed in the present work is comprised of $64 \times 65 \times 64$ nodes with trilinear hexahedral elements, while the LES reference data was obtained using $128 \times 97 \times 128$ nodes employing spectral interpolation. To further evaluate the effectiveness of the proposed model, we focus on the near wall region and present the non-dimensional mean profile of velocity and temperature fields on a log scale (see Fig. 26). In both viscous and conductive sub-layers, the mean profile of the flow fields is very close to the resolved DNS solution. We also present quantitative comparisons of the second order statistics from our model by plotting the root-mean-square of fluctuations of the flow fields and the fluxes, including streamwise/wall-normal/spanwise velocities (i.e., $\langle u' \rangle$, $\langle v' \rangle$, $\langle w' \rangle$), temperature (i.e., $\langle \theta' \rangle$), thermal flux (i.e., $\langle \theta' v' \rangle$) and the off-diagonal term of Reynolds stresses (i.e., $\langle u' v' \rangle$)

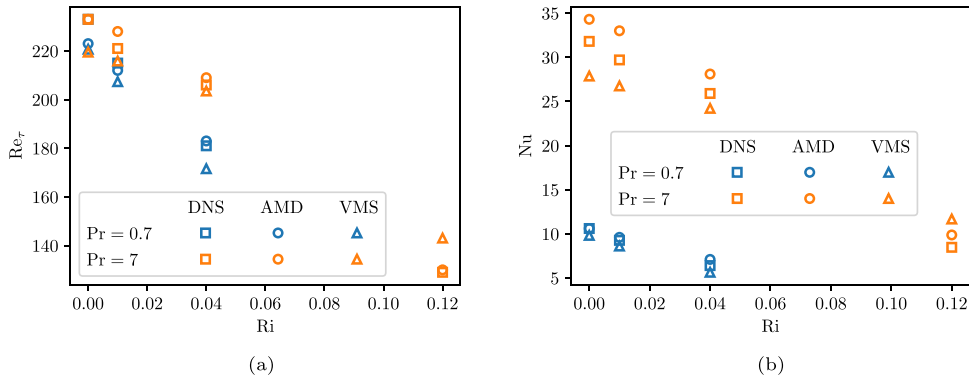


Fig. 24. Comparison of the friction Reynolds number Re_τ and Nusselt number Nu with varying Richardson number and Prandtl number: DNS [66] (squares), LES [71] (circles) and LES (present work) (triangles); $Pr = 0.7$ (blue) and $Pr = 7$ (orange). (For interpretation of the references to color in this figure legend, the reader is referred to the web version of this article.)

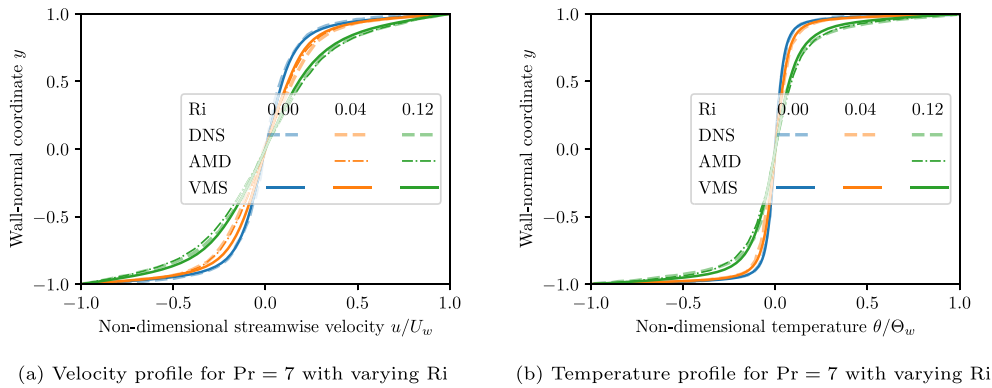


Fig. 25. Flow profiles of time-space averaged streamwise velocity and temperature with fixed $Pr = 7$ but varying Ri : case B1, B2 and B4.

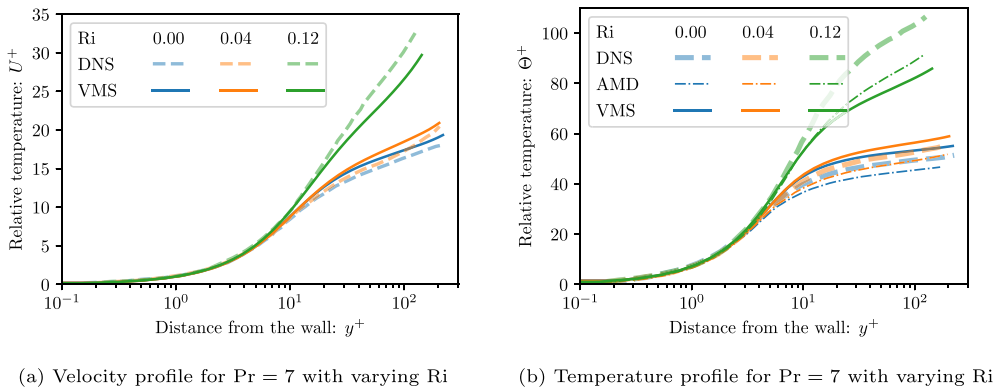


Fig. 26. Flow profiles of time-space averaged streamwise velocity and temperature with fixed $Pr = 7$ but varying Ri in the near-wall region with log scale: case B1, B2 and B4.

in Fig. 27. As compared with the coarse mesh, results obtained on the finer mesh are uniformly close to the DNS data that shows variational convergence feature of the model.

Stable stratification that results from the counteracting effects of the background temperature gradient, and the direction of the gravitational acceleration can dissipate the smaller turbulent structures in the flow, and is called re-laminarization. One issue with the traditional viscosity-based models for LES is the viscous dissipation that still

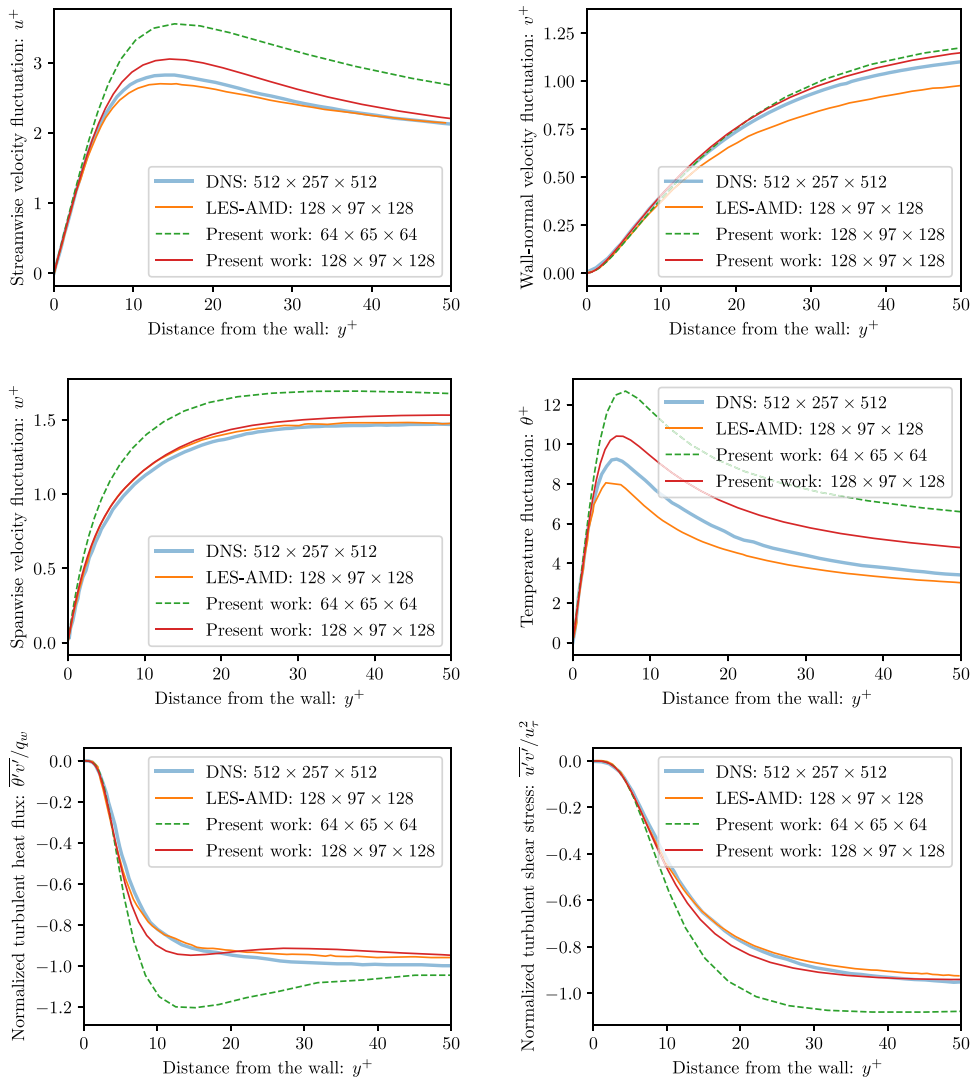


Fig. 27. Second-order statistics of flow fields in turbulent Couette flow: cases B3C and B3F.

persists even when the flow has re-entered the laminar regime. This excessive viscosity can inevitably amplify the re-laminarization effect, thereby affecting the spatial and temporal accuracy of the large eddies in the flow. On the other hand, the DNS data with the same governing parameters may still show observable turbulence. The numerical tests carried out in this section show that the proposed VMS-based model does not have spurious viscous dissipation. Unlike the reference LES work [71], where the mesh is refined in the wall-normal direction to prevent non-physical re-laminarization, none of the test cases presented in our study needed any local refinement for the given Pr and with varying Ri . To qualitatively describe the re-laminarization due to stable stratification, the distribution of temperature field in the x - z plane at $y^+ = 5$ for $Pr = 7$, but with varying the Ri , is presented in Fig. 28. With increasing Ri , the stripe-type distribution of temperature field in the near wall region gets further elongated. These transitions become more explicit in Fig. 28(d), where strong stratification almost eliminates most of the temperature fluctuations. Finally, we present the overall flow structure in Fig. 29 via volume rendering of the instantaneous temperature and velocity fields near the top and the bottom planes, along with the plotting of the streamlines to illustrate the flow fields in the core region.

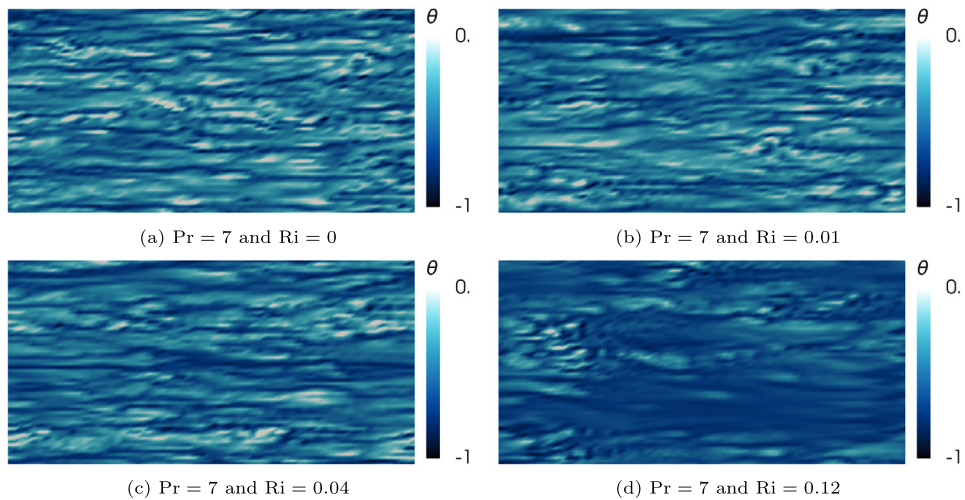


Fig. 28. Temperature field at the wall-normal plane at $y^+ = 5$ with different Ri .

6. Conclusions

We have presented a residual-based turbulence model for density stratified incompressible flows that dynamically adapts to the local residuals, thereby providing a two-way coupled interaction between resolved and unresolved scales. The main contribution of the paper is a systematic and consistent derivation of the fine-scale closure model that is free of any tunable parameters. A hierarchical application of VMS method leads to hierarchically coupled fine-scale variational equations. A direct application of bubble functions approach to resolve the fine-scale variational equations is the key to the derivation of the fine-scale models that are nonlinear and time-dependent. Embedding the derived model from the level-II variational equation in the level-I variational equation results in a stabilized mixed-field subproblem. The enhanced stability of the level-I equations helps in locally resolving the unconstrained level-I system of equations that is driven by the residual of Euler–Lagrange equations emanating from the conservation of mass, momentum, and energy. This results in variational consistency of the residual-based turbulence model that ensures that the turbulence model vanishes uniformly when the flow ceases to be turbulent and the computed coarse scales comprise all the flow physics. The transient linearized fine-scale model leads to consistently linearized tangent operator that is essential in achieving quadratic convergence in the nonlinear solution scheme. Numerical test cases show that the derived large eddy turbulence model accommodates forward- and back-scatter of energy and entropy and effectively embeds sub-grid scale physics in the computable scales of the problem to yield economic solutions for turbulent flows on cruder spatial discretizations.

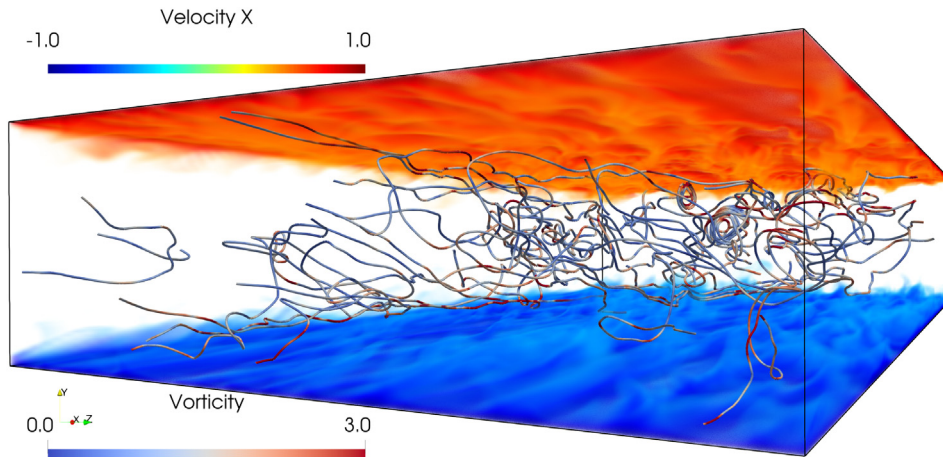
Declaration of competing interest

The authors declare that they have no known competing financial interests or personal relationships that could have appeared to influence the work reported in this paper.

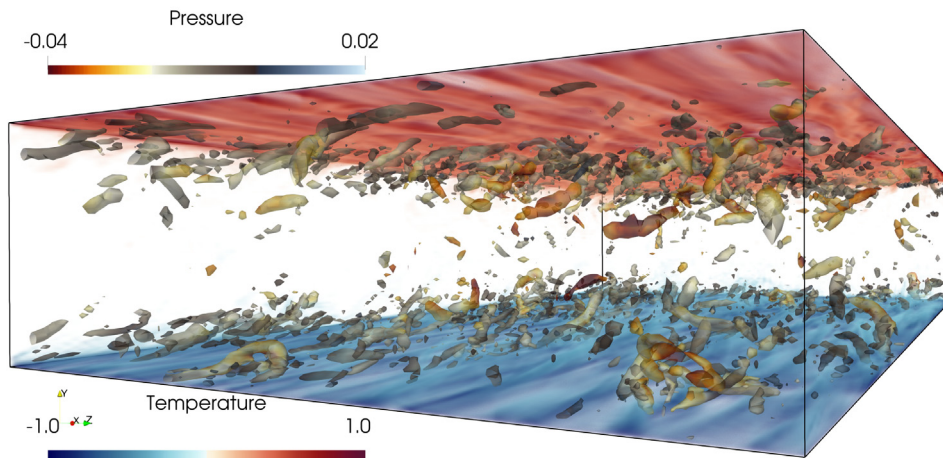
Acknowledgments

This work was supported by US-NSF grant NSF-DMS-16-20231 to the University of Illinois. L.Z. was partially supported by the NSFC Basic Science Center Program for “Multiscale Problems in Nonlinear Mechanics” (Grant No. 11988102). This support is gratefully acknowledged.

This research is part of the Blue Waters sustained-petascale computing project, which is supported by the National Science Foundation (awards OCI-0725070 and ACI-1238993) the State of Illinois. Blue Waters is a joint effort of the University of Illinois at Urbana-Champaign and its National Center for Supercomputing Applications.



(a) Streamwise velocity field (volume rendered) at the top and bottom boundary layers and velocity streamlines colored by the magnitude of vorticity in the core region



(b) Temperature field (volume rendered) at the bottom boundary layer and isosurfaces of Q-criterion colored by the distance from the top wall

Fig. 29. Instantaneous flow structures in turbulent Couette flows. (For interpretation of the references to color in this figure legend, the reader is referred to the web version of this article.)

Appendix A. Algebraic structure of the stability tensors

The solution process illustrated in Algorithm 1 can be embedded in a standard finite-element program by implementing the corresponding consistent tangent and the residual vector from the proposed weak form presented in Eq. (56). This appendix shows the details of the construction of the element-level contributions to the consistent tangent and residual vector of the discrete system for a typical iteration $i + 1$ within a Newton–Raphson loop advancing from time-step n to $n + 1$. As presented in Algorithm 1, we assume that the solution fields and their time derivatives at iteration i (i.e., $\mathbf{u}_{(i)}^{(n+1)}$, $p_{(i)}^{(n+1)}$, $\theta_{(i)}^{(n+1)}$, $\mathbf{u}_{,t(i)}^{(n+1)}$ and $\theta_{,t(i)}^{(n+1)}$) are available. For brevity of presentation, the subscripts and superscripts denoting the time-step and iteration number are neglected hereon.

A.1. Fine-scale stability tensor

The tensor $\boldsymbol{\tau}'$ that variationally scales the residuals from the preceding levels and projects them back onto the level-II fine-scale problems is written as follows

$$\boldsymbol{\tau}' = b_{\parallel}^e \boldsymbol{\tau}'^e \tag{A.1}$$

where $\boldsymbol{\tau}'^e$ is comprised of the coefficients of the solution of fine-scale level-II linear system in Eq. (39) at the corresponding virtual node. The explicit form of the linear system that is evaluated element-wise is as follows.

$$\left(\frac{\alpha_m}{\alpha_f \gamma \Delta t} \mathbf{M}'_{\parallel} + \mathbf{K}'_{\parallel}{}^{\text{ADV}} + \mathbf{K}'_{\parallel}{}^{\text{DIFF}} + \mathbf{K}'_{\parallel}{}^{\text{STRA}} \right) \boldsymbol{\tau}'^e = \mathbf{R}'_{\parallel} \tag{A.2}$$

where $\mathbf{M}'_{\parallel} = (b_{\parallel}^e, b_{\parallel}^e) \mathbf{I}_{4 \times 4}$ denotes the mass matrix; $\mathbf{R}'_{\parallel} = (b_{\parallel}^e, 1) \mathbf{I}_{4 \times 4}$ denotes the RHS matrix; $\mathbf{K}'_{\parallel}{}^{\text{ADV}}$, $\mathbf{K}'_{\parallel}{}^{\text{DIFF}}$ and $\mathbf{K}'_{\parallel}{}^{\text{STRA}}$ denote the stiffness matrix contribution from the advection, diffusion and stratification components, respectively. The corresponding expressions are as follows

$$\begin{aligned} \mathbf{K}'_{\parallel}{}^{\text{ADV}} &= (b_{\text{adv}}^e, \mathbf{u} \cdot \nabla b_{\parallel}^e) \mathbf{I}_{4 \times 4} + \begin{bmatrix} (b_{\parallel}^e, \nabla^T \mathbf{u} b_{\parallel}^e)_{(3 \times 3)} & \mathbf{0}_{(3 \times 1)} \\ (b_{\parallel}^e, \nabla^T \theta b_{\parallel}^e)_{(1 \times 3)} & 0 \end{bmatrix} \\ \mathbf{K}'_{\parallel}{}^{\text{DIFF}} &= \nu \begin{bmatrix} (\nabla b_{\parallel}^e, \nabla^T b_{\parallel}^e)_{(3 \times 3)} & \mathbf{0}_{(3 \times 1)} \\ \mathbf{0}_{(1 \times 3)} & 0 \end{bmatrix} + \begin{bmatrix} \nu (\nabla b_{\parallel}^e, \nabla b_{\parallel}^e) \mathbf{I}_{(3 \times 3)} & \mathbf{0}_{(3 \times 1)} \\ \mathbf{0}_{(1 \times 3)} & \alpha (\nabla b_{\parallel}^e, \nabla b_{\parallel}^e) \end{bmatrix} \\ \mathbf{K}'_{\parallel}{}^{\text{STRA}} &= \beta \begin{bmatrix} \mathbf{0}_{(3 \times 3)} & (b_{\parallel}^e, b_{\parallel}^e) \hat{\mathbf{g}}_{(3 \times 1)} \\ \mathbf{0}_{(1 \times 3)} & 0 \end{bmatrix} \end{aligned} \tag{A.3}$$

Remark 12. We are solving Eq. (A.2) for tensorial form of $\boldsymbol{\tau}'^e$ without the use of the Voigt notation.

A.2. Coarse-scale stability tensor

The coarse-scale stability tensor $\boldsymbol{\tau}$ that multiplies the residual of Euler–Lagrange equations at coarse scale level is written as follows

$$\boldsymbol{\tau} = b_1^e \boldsymbol{\tau}^e \tag{A.4}$$

where $\boldsymbol{\tau}^e$ is the solution of the element-wise stabilized fine-scale level-I linearized system in Eq. (52) at the corresponding virtual node. The explicit form of the linearized system is

$$\begin{aligned} \left\{ \frac{\alpha_m}{\alpha_f \gamma \Delta t} \left(\mathbf{M}'_1{}^{\text{Gal}} - \int_{\Omega^e} \mathbf{X}' \boldsymbol{\tau}' \mathbf{R}'_m d\Omega \right) + \left(\mathbf{K}'_1{}^{\text{Gal}} - \int_{\Omega^e} \mathbf{X}' \boldsymbol{\tau}' \mathbf{R}'_s d\Omega \right) \right\} \boldsymbol{\tau}^e \\ = \left(\mathbf{R}'_1{}^{\text{Gal}} - \int_{\Omega^e} \mathbf{X}' \boldsymbol{\tau}' \mathbf{1}' d\Omega \right) \end{aligned} \tag{A.5}$$

where $\mathbf{M}'_1{}^{\text{Gal}}$, $\mathbf{K}'_1{}^{\text{Gal}}$ and $\mathbf{R}'_1{}^{\text{Gal}} = (b_1^e, 1) \mathbf{I}_{(5 \times 5)}$ are the mass and stiffness matrices and the residual of the Galerkin part in the stabilized weak form, respectively; \mathbf{X}' is the weighting matrix for the stabilization terms; and \mathbf{R}'_m and \mathbf{R}'_s are the matrix form of transient and steady-state parts of the Euler–Lagrange equations of the linearized fine-scale level-I in Eq. (36), respectively. The Galerkin part in Eq. (52) contributes to the same slots as in Eq. (39), however it is expanded via bubble functions that are linearly independent of the functions employed at level-II. The resulting explicit forms are as follows.

$$\mathbf{M}'_1{}^{\text{Gal}} = (b_1^e, b_1^e) \begin{bmatrix} \mathbf{I}_{(3 \times 3)} & & \\ & 0 & \\ & & 1 \end{bmatrix} \tag{A.6}$$

$$\mathbf{K}'_{\text{I Gal}} = \left[\begin{array}{c|c|c} (b_1^e, \mathbf{u} \cdot \nabla b_1^e) \mathbf{I}_{(3 \times 3)} \\ + (b_1^e, b_1^e \nabla^T \mathbf{u})_{(3 \times 3)} \\ + \nu (\nabla b_1^e, \nabla^T b_1^e)_{(3 \times 3)} \\ + \nu (\nabla b_1^e, \nabla b_1^e) \mathbf{I}_{(3 \times 3)} \\ \hline (b_1^e, \nabla^T b_1^e)_{(1 \times 3)} \\ \hline (b_1^e, b_1^e \nabla^T \theta)_{(1 \times 3)} \end{array} \middle| \begin{array}{c} (-b_1^e, \nabla b_1^e)_{(3 \times 1)} \\ \\ 0 \\ 0 \end{array} \middle| \begin{array}{c} (b_1^e, \beta \hat{\mathbf{g}} b_1^e)_{(3 \times 1)} \\ \\ 0 \\ (b_1^e, \mathbf{u} \cdot \nabla b_1^e) + \alpha (\nabla b_1^e, \nabla b_1^e) \end{array} \right] \quad (\text{A.7})$$

The matrix form of the weighting matrix \mathbf{X}' is derived by taking variational derivative of Eq. (49a) with respect to the fine-scale level-I weighting functions \mathbf{W}'_{I} , namely,

$$\mathbf{X}'_{(5 \times 4)} = \frac{\partial [\chi'_M, \chi'_E]}{\partial \mathbf{W}'_{\text{I}}} = \left[\begin{array}{c|c} -\mathbf{u} \cdot \nabla b_1^e \mathbf{I}_{(3 \times 3)} + b_1^e \nabla^T \mathbf{u}_{(3 \times 3)} \\ -\nu ((\nabla \otimes \nabla)_{(3 \times 3)} b_1^e + \Delta b_1^e \mathbf{I}_{(3 \times 3)}) \\ \hline -(\nabla^T)_{(1 \times 3)} b_1^e \\ \hline b_1^e (\nabla^T)_{(1 \times 3)} \theta \end{array} \middle| \begin{array}{c} b_1^e \beta \hat{\mathbf{g}}_{(3 \times 1)} \\ 0 \\ -\mathbf{u} \cdot \nabla b_1^e - \alpha \Delta b_1^e \end{array} \right] \quad (\text{A.8})$$

Likewise, \mathbf{R}'_m and \mathbf{R}'_s are derived by taking variational derivatives of Eq. (36) with respect to the transient and steady-state weighting functions as follows

$$\mathbf{R}'_{m(4 \times 5)} = \frac{\partial [\mathbf{r}'_M, \mathbf{r}'_E]}{\partial [\mathbf{u}'_{1,t}, p'_{1,t}, \theta'_{1,t}]^T} = \left[\begin{array}{c|c|c} b_1^e \mathbf{I}_{(3 \times 3)} & \mathbf{0}_{(3 \times 1)} & \mathbf{0}_{(3 \times 1)} \\ \hline \mathbf{0}_{(1 \times 3)} & 0 & b_1^e \end{array} \right] \quad (\text{A.9})$$

$$\mathbf{R}'_{s(4 \times 5)} = \frac{\partial [\mathbf{r}'_M - \mathbf{u}'_{1,t}, \mathbf{r}'_E - \theta'_{1,t}]}{\partial [\mathbf{u}'_1, p', \theta'_1]^T} = \left[\begin{array}{c|c|c} \mathbf{u} \cdot \nabla b_1^e \mathbf{I}_{(3 \times 3)} \\ + b_1^e (\nabla^T \mathbf{u})_{(3 \times 3)} \\ -\nu (\nabla \otimes \nabla)_{(3 \times 3)} b_1^e \\ + \Delta b_1^e \mathbf{I}_{(3 \times 3)} \\ \hline b_1^e (\nabla^T)_{(1 \times 3)} \theta \end{array} \middle| \begin{array}{c} (\nabla)_{(3 \times 1)} b_1^e \\ 0 \\ \mathbf{u} \cdot \nabla b_1^e - \alpha \Delta b_1^e \end{array} \middle| \begin{array}{c} b_1^e \beta \hat{\mathbf{g}}_{(3 \times 1)} \end{array} \right] \quad (\text{A.10})$$

Finally, applying the mean projection theorem to the coarse-scale residual results in $\mathbf{1}'$ in Eq. (A.5), which takes the following form

$$\mathbf{1}'_{(4 \times 5)} = \left[\begin{array}{c|c|c} \mathbf{I}_{(3 \times 3)} & \mathbf{0}_{(3 \times 1)} & \mathbf{0}_{(3 \times 1)} \\ \hline \mathbf{0}_{(1 \times 3)} & 0 & 1 \end{array} \right] \quad (\text{A.11})$$

Remark 13. Mathematical stability of the method necessitates that the spaces for the fine-scale enrichment functions employed at level-I and level-II, as well as the finite element function spaces employed at the global level should be mutually linearly independent.

Appendix B. Estimation of the computational cost

The computational cost within a single iteration of a Newton–Raphson loop, as shown in Algorithm 1, can be divided into two parts: (i) the evaluation and assembly process, where the element-wise consistent tangents and residuals are integrated and then assembled into the global linear system, and (ii) the solution process where the global linear system is solved for the increment in the solution fields. As shown in the derived algebraic form of the fine-scale solutions in Eq. (53) and the final stabilized form in Eq. (56), all the fine-scale related terms are implicitly expressed in terms of the residuals of the coarse-scale Euler–Lagrange equations, premultiplied by the stability tensor. The residuals of the Euler–Lagrange equations are expanded in terms of the shape functions employed at the coarse scale level. It is only the stability tensors (i.e., $\boldsymbol{\tau}$ and $\boldsymbol{\tau}'$) that are functions of the fine-scale basis functions employed for the expansion of the fine-scale fields. The importance of employing bubble functions that are non-zero within the element and become zero at the element edges becomes apparent now. Since bubble functions render the calculation of $\boldsymbol{\tau}$ and $\boldsymbol{\tau}'$ a local problem, the process is not only embarrassingly parallel, it also does not involve any passing of data between the elements. Once the stability tensors are evaluated at the virtual

Table B.1

Estimation of the relative cost in the numerical integration of the stability tensors (p : order of the shape function, p^{int} : highest order of monomials in the integrand, n^{GP} : number of quadrature points in 1D, n^{el} : number of shape functions per element, n_f : cost factor, and cost is scaled by $(n_C^{\text{GP}})^{-3}(n_C^{\text{el}})^{-2}$).

(a) 8-node hexahedron						
	p	p^{int}	n^{GP}	n^{el}	n_f	Scaled cost
Coarse	1	5	3	8	1	1
Fine-I	2	8	5	1	1	7.23%
Fine-II	4	8	5	1	0.5	3.62%
(b) 27-node hexahedron						
	p	p^{int}	n^{GP}	n^{el}	n_f	Scaled cost
Coarse	2	12	7	27	1	1
Fine-I	4	16	9	1	1	0.292%
Fine-II	6	13	7	1	0.5	0.0686%

nodes, the cost associated with numerical integration of the fine-scale terms in Eq. (56) is similar to that of the integration of the standard Galerkin terms because these Euler–Lagrange residuals are represented via the same Lagrange shape functions that are employed in the evaluation of the Galerkin terms. Furthermore, the bandwidth of the global consistent tangent and the number of the nodal unknowns at the global level remain the same in either two-level VMS method or the three-level VMS method.

The computation of the spatiotemporally adaptive stability tensor τ' and τ , as shown in lines 6 and 7 in Algorithm 1 involves two quadrature loops and two local linear system solution processes. Other than these two steps that locally and dynamically evaluate the stability tensors, the cost of computation of the rest of the algorithm is identical to that of any standard stabilized method. To quantitatively evaluate the cost of floating point operations in the numerical integration, we take a p_C -order hexahedral element as an example. The number of shape functions (nodes) n^{el} in a hexahedral element is $n^{\text{el}} = (p_C + 1)^{n_{sd}}$, where $n_{sd} = 3$ is the number of dimensions of the problem. The fine scale level-I bubble function is taken as the order p_{F_I} , which is equal to the smallest even number that is greater than p_C , and the fine scale level-II bubble function takes the order of $p_{F_{II}} = p_{F_I} + 2$. The highest order terms and their order of polynomials that are to be integrated p^{int} at each scale are estimated as follows:

1. Coarse scale: $(\mathbf{u}' \cdot \nabla \bar{\mathbf{w}}, \boldsymbol{\tau} \bar{\mathbf{u}} \cdot \nabla \bar{\mathbf{u}}) \rightarrow 3p_C + 2p_{F_I} - 2$
2. Fine scale level-I: $(\bar{\mathbf{u}} \cdot \nabla \mathbf{w}'_I, \boldsymbol{\tau}' \bar{\mathbf{u}} \cdot \nabla \mathbf{u}'_I) \rightarrow 2p_C + 3p_{F_I}$
3. Fine scale level-II: $(\mathbf{w}'_{II}, \bar{\mathbf{u}} \cdot \nabla \mathbf{u}'_{II}) \rightarrow p_C + 2p_{F_I} + 3$

We denote the Gaussian quadrature point along one dimension of a hexahedral element employed in the evaluation of element level quantities at the coarse scale level, level-I fine scales, and level-II fine scales as n_C^{GP} , $n_{F_I}^{\text{GP}}$ and $n_{F_{II}}^{\text{GP}}$, respectively, which are determined by the highest order monomial in the integrand at the corresponding level.

Due to the hierarchical application of VMS scale-split, the number and the forms of terms are almost identical between the coarse scales in Eq. (56) and level-I fine scales in Eq. (50). The fine scale level-II weak form in Eq. (35) contains only half of the terms (i.e., only the Galerkin terms). It is reasonable to set the computational cost to evaluate the standard stabilized weak form (of coarse-scale) for a single shape function at a given (by otherwise arbitrary) Gaussian point as a base unit, and denoted as n_f . We further assume that such an evaluation of the stabilized weak form of fine scale level-I is also 1 unit, and that of the fine scale level-II weak form is 0.5 unit. It is worth noticing that this assumption overestimates the computational cost at the fine-scale levels because the nonlinear terms have been linearized at the fine levels. The number of terms n_{term} that need to be evaluated is $n_{\text{term}} = (n^{\text{el}} n_{sd})^2 + (n^{\text{el}} n_{sd})$, which consists of the components in the consistent tangent and the residual. We can estimate the additional cost associated with the integration at either of the fine-scale levels as follows.

$$n_{\text{term}} (n^{\text{GP}})^{n_{sd}} n_f \approx (n^{\text{el}})^2 (n^{\text{GP}})^{n_{sd}} n_f \tag{B.1}$$

The estimated costs to construct linear systems for the two fine-scale levels that correspond to the cases of 8-node or 27-node hexahedral elements employed for coarse-scale discretization are shown in Tables B.1a and B.1b,

respectively. As compared to standard stabilized method, multilevel VMS method only introduces an additional 10 percent computational cost in the integration process for the case of trilinear hexahedra. For the 27-node hexahedra, the additional cost is further reduced to less than 0.4 percent. The size of the element-wise linear systems of two fine-scale levels in Eqs. (39) and (52) are $n_{sd} + 1$ and $n_{sd} + 2$, respectively. The cost of solving a $n \times n$ system with a direct solver is approximately $O(n^3)$. Therefore, the computational cost for solving this small local linear system is negligibly small as compared to the cost associated with the numerical integration of the element consistent tangent and residual vector.

Consequently, the multi-level VMS method only introduces a slight increase in the computational cost in the element-wise integration process, as compared to the standard stabilized methods. In addition, the process is perfectly parallelizable, and does not involve inter-element data communication. Since the element integration process only cost less than 25 percent of the total compute time in large simulation [72], with a net 2.5 percent increase (10 percent of 25 percent for trilinear hexahedron) in the formation of the algebraic system, we develop a residual-based LES method which is free of any *ad hoc* parameter dependent turbulence models.

References

- [1] P. Sagaut, Large Eddy Simulation for Incompressible Flows: An Introduction, Springer Science & Business Media, 2006, <http://dx.doi.org/10.1007/b137536>.
- [2] G. Boffetta, A. Mazzino, Incompressible Rayleigh–Taylor turbulence, Annu. Rev. Fluid Mech. 49 (1) (2017) 119–143, <http://dx.doi.org/10.1146/annurev-fluid-010816-060111>.
- [3] R.W. Bilger, Turbulent diffusion flames, Annu. Rev. Fluid Mech. 21 (1) (1989) 101–135, <http://dx.doi.org/10.1146/annurev.fl.21.010189.000533>.
- [4] I.B. Zeldovich, A.A. Ruzmaikin, D.D. Sokolov, Magnetic Fields in Astrophysics, Vol. 3, Gordon and Breach Science Publishers, New York, 1983.
- [5] A.W. Woods, Turbulent plumes in nature, Annu. Rev. Fluid Mech. 42 (1) (2010) 391–412, <http://dx.doi.org/10.1146/annurev-fluid-121108-145430>.
- [6] M. Ardyna, L. Lacour, S. Sergi, F. d’Ovidio, J.-B. Sallée, M. Rembauville, S. Blain, A. Tagliabue, R. Schlitzer, C. Jeandel, K.R. Arrigo, H. Claustre, Hydrothermal vents trigger massive phytoplankton blooms in the Southern Ocean, Nature Commun. 10 (1) (2019) 1–8, <http://dx.doi.org/10.1038/s41467-019-09973-6>.
- [7] S.M. Glenn, T.N. Miles, G.N. Seroka, Y. Xu, R.K. Forney, F. Yu, H. Roarty, O. Schofield, J. Kohut, Stratified coastal ocean interactions with tropical cyclones, Nature Commun. 7 (1) (2016) 1–10, <http://dx.doi.org/10.1038/ncomms10887>.
- [8] C. Garnier, J. Currie, T. Muneer, Integrated collector storage solar water heater: Temperature stratification, Appl. Energy 86 (9) (2009) 1465–1469, <http://dx.doi.org/10.1016/j.apenergy.2008.12.009>.
- [9] V. Armenio, S. Sarkar, An investigation of stably stratified turbulent channel flow using large-eddy simulation, J. Fluid Mech. 459 (2002) 1–42, <http://dx.doi.org/10.1017/S0022112002007851>.
- [10] G. Ivey, K. Winters, J. Koseff, Density stratification, turbulence, but how much mixing? Annu. Rev. Fluid Mech. 40 (1) (2008) 169–184, <http://dx.doi.org/10.1146/annurev.fluid.39.050905.110314>.
- [11] S. Pirozzoli, M. Bernardini, R. Verzicco, P. Orlandi, Mixed convection in turbulent channels with unstable stratification, J. Fluid Mech. 821 (2017) 482–516, <http://dx.doi.org/10.1017/jfm.2017.216>.
- [12] S.B. Pope, Turbulent Flows, IOP Publishing, 2001.
- [13] A. Garanaik, S.K. Venayagamoorthy, Assessment of small-scale anisotropy in stably stratified turbulent flows using direct numerical simulations, Phys. Fluids 30 (12) (2018) 126602, <http://dx.doi.org/10.1063/1.5055871>.
- [14] D. Lohse, K.-Q. Xia, Small-scale properties of turbulent Rayleigh–Bénard convection, Annu. Rev. Fluid Mech. 42 (1) (2010) 335–364, <http://dx.doi.org/10.1146/annurev.fluid.010908.165152>.
- [15] W.D. Smyth, J.N. Moum, Anisotropy of turbulence in stably stratified mixing layers, Phys. Fluids 12 (6) (2000) 1343–1362, <http://dx.doi.org/10.1063/1.870386>.
- [16] M. Germano, U. Piomelli, P. Moin, W.H. Cabot, A dynamic subgrid-scale eddy viscosity model, Phys. Fluids A 3 (7) (1991) 1760–1765, <http://dx.doi.org/10.1063/1.857955>.
- [17] S. Khani, M.L. Waite, Large eddy simulations of stratified turbulence: The dynamic Smagorinsky model, J. Fluid Mech. 773 (2015) 327–344, <http://dx.doi.org/10.1017/jfm.2015.249>.
- [18] S. Remmler, S. Hickel, Direct and large eddy simulation of stratified turbulence, Int. J. Heat Fluid Flow 35 (2012) 13–24, <http://dx.doi.org/10.1016/j.ijheatfluidflow.2012.03.009>.
- [19] V.C. Wong, D.K. Lilly, A comparison of two dynamic subgrid closure methods for turbulent thermal convection, Phys. Fluids 6 (2) (1994) 1016–1023, <http://dx.doi.org/10.1063/1.868335>.
- [20] C. Meneveau, T.S. Lund, W.H. Cabot, A Lagrangian dynamic subgrid-scale model of turbulence, J. Fluid Mech. 319 (-1) (1996) 353, <http://dx.doi.org/10.1017/S0022112096007379>.
- [21] V. Yakhot, S.A. Orszag, Renormalization group analysis of turbulence. I. Basic theory, J. Sci. Comput. 1 (1) (1986) 3–51, <http://dx.doi.org/10.1007/BF01061452>.
- [22] W.D. McComb, Homogeneous, Isotropic Turbulence: Phenomenology, Renormalization and Statistical Closures, Vol. 162, OUP Oxford, 2014, <http://dx.doi.org/10.1093/acprof:oso/9780199689385.001.0001>.

- [23] S. Vashishtha, M.K. Verma, R. Samuel, Large-eddy simulations of turbulent thermal convection using renormalized viscosity and thermal diffusivity, *Phys. Rev. E* 98 (4) (2018) 043109, <http://dx.doi.org/10.1103/PhysRevE.98.043109>.
- [24] I. Akkerman, Y. Bazilevs, V.M. Calo, T.J.R. Hughes, S. Hulshoff, The role of continuity in residual-based variational multiscale modeling of turbulence, *Comput. Mech.* 41 (3) (2008) 371–378, <http://dx.doi.org/10.1007/s00466-007-0193-7>.
- [25] Y. Bazilevs, V.M. Calo, J.A. Cottrell, T.J.R. Hughes, A. Reali, G. Scovazzi, Variational multiscale residual-based turbulence modeling for large eddy simulation of incompressible flows, *Comput. Methods Appl. Mech. Engrg.* 197 (1) (2007) 173–201, <http://dx.doi.org/10.1016/j.cma.2007.07.016>.
- [26] R. Calderer, A. Masud, Residual-based variational multiscale turbulence models for unstructured tetrahedral meshes, *Comput. Methods Appl. Mech. Engrg.* 254 (2013) 238–253, <http://dx.doi.org/10.1016/j.cma.2012.09.015>.
- [27] R. Calderer, L. Zhu, R. Gibson, A. Masud, Residual-based turbulence models and arbitrary Lagrangian–Eulerian framework for free surface flows, *Math. Models Methods Appl. Sci.* 25 (12) (2015) 2287–2317, <http://dx.doi.org/10.1142/S0218202515400096>.
- [28] T.J.R. Hughes, Multiscale phenomena: Green’s functions, the Dirichlet-to-Neumann formulation, subgrid scale models, bubbles and the origins of stabilized methods, *Comput. Methods Appl. Mech. Engrg.* 127 (1) (1995) 387–401, [http://dx.doi.org/10.1016/0045-7825\(95\)00844-9](http://dx.doi.org/10.1016/0045-7825(95)00844-9).
- [29] T.J.R. Hughes, L. Mazzei, K.E. Jansen, Large Eddy Simulation and the variational multiscale method, *Comput. Vis. Sci.* 3 (1–2) (2000) 47–59, <http://dx.doi.org/10.1007/s007910050051>.
- [30] T.J.R. Hughes, L. Mazzei, A.A. Oberai, A.A. Wray, The multiscale formulation of large eddy simulation: Decay of homogeneous isotropic turbulence, *Phys. Fluids* 13 (2) (2001) 505–512, <http://dx.doi.org/10.1063/1.1332391>.
- [31] T.J.R. Hughes, A.A. Oberai, L. Mazzei, Large eddy simulation of turbulent channel flows by the variational multiscale method, *Phys. Fluids* 13 (6) (2001) 1784–1799, <http://dx.doi.org/10.1063/1.1367868>.
- [32] A. Masud, R. Calderer, A variational multiscale stabilized formulation for the incompressible Navier–Stokes equations, *Comput. Mech.* 44 (2) (2009) 145–160, <http://dx.doi.org/10.1007/s00466-008-0362-3>.
- [33] A. Masud, R. Calderer, A variational multiscale method for incompressible turbulent flows: Bubble functions and fine scale fields, *Comput. Methods Appl. Mech. Engrg.* 200 (33) (2011) 2577–2593, <http://dx.doi.org/10.1016/j.cma.2011.04.010>.
- [34] G. Volker, W.W. A., R. Ekkehard, Large eddy simulation of turbulent incompressible flows by a three-level finite element method, *Internat. J. Numer. Methods Fluids* 48 (10) (2005) 1067–1099, <http://dx.doi.org/10.1002/fld.961>.
- [35] P. Gamnitzer, V. Gravemeier, W.A. Wall, Time-dependent subgrid scales in residual-based large eddy simulation of turbulent channel flow, *Comput. Methods Appl. Mech. Engrg.* 199 (13) (2010) 819–827, <http://dx.doi.org/10.1016/j.cma.2009.07.009>.
- [36] M.-C. Hsu, Y. Bazilevs, V. Calo, T. Tezduyar, T. Hughes, Improving stability of stabilized and multiscale formulations in flow simulations at small time steps, *Comput. Methods Appl. Mech. Engrg.* 199 (13) (2010) 828–840, <http://dx.doi.org/10.1016/j.cma.2009.06.019>.
- [37] A. Masud, L. Zhu, Variationally derived closure models for large eddy simulation of incompressible turbulent flows, *Internat. J. Numer. Methods Fluids* 93 (7) (2021) 2089–2120, <http://dx.doi.org/10.1002/fld.4966>.
- [38] N. Ahmed, T.C. Rebollo, V. John, S. Rubino, A review of variational multiscale methods for the simulation of turbulent incompressible flows, *Arch. Comput. Methods Eng.* 24 (1) (2017) 115–164, <http://dx.doi.org/10.1007/s11831-015-9161-0>.
- [39] S. Xu, B. Gao, M.-C. Hsu, B. Ganapathysubramanian, A residual-based variational multiscale method with weak imposition of boundary conditions for buoyancy-driven flows, *Comput. Methods Appl. Mech. Engrg.* 352 (2019) 345–368, <http://dx.doi.org/10.1016/j.cma.2019.03.057>.
- [40] S. Xu, N. Liu, J. Yan, Residual-based variational multi-scale modeling for particle-laden gravity currents over flat and triangular wavy terrains, *Comput. & Fluids* 188 (2019) 114–124, <http://dx.doi.org/10.1016/j.compfluid.2019.05.008>.
- [41] J. Yan, A. Korobenko, A.E. Tejada-Martínez, R. Golshan, Y. Bazilevs, A new variational multiscale formulation for stratified incompressible turbulent flows, *Comput. & Fluids* 158 (2017) 150–156, <http://dx.doi.org/10.1016/j.compfluid.2016.12.004>.
- [42] R. Codina, J. Principe, M. Ávila, Finite element approximation of turbulent thermally coupled incompressible flows with numerical sub-grid scale modelling, *Internat. J. Numer. Methods Heat Fluid Flow* 20 (5) (2010) 492–516, <http://dx.doi.org/10.1108/09615531011048213>.
- [43] G.M. Guerra, S. Zio, J.J. Camata, F.A. Rochinha, R.N. Elias, P.L.B. Paraizo, A.L.G.A. Coutinho, Numerical simulation of particle-laden flows by the residual-based variational multiscale method, *Internat. J. Numer. Methods Fluids* 73 (8) (2013) 729–749, <http://dx.doi.org/10.1002/fld.3820>.
- [44] A. Masud, R. Calderer, Residual-based turbulence models for moving boundary flows: Hierarchical application of variational multiscale method and three-level scale separation, *Internat. J. Numer. Methods Fluids* 73 (3) (2013) 284–305, <http://dx.doi.org/10.1002/fld.3801>.
- [45] A. Masud, L.P. Franca, A hierarchical multiscale framework for problems with multiscale source terms, *Comput. Methods Appl. Mech. Engrg.* 197 (33) (2008) 2692–2700, <http://dx.doi.org/10.1016/j.cma.2007.12.024>.
- [46] L. Zhu, A. Goraya Shoaib, A. Masud, Interface-capturing method for free-surface plunging and breaking waves, *J. Eng. Mech.* 145 (11) (2019) 04019088, [http://dx.doi.org/10.1061/\(ASCE\)EM.1943-7889.0001641](http://dx.doi.org/10.1061/(ASCE)EM.1943-7889.0001641).
- [47] L. Zhu, A. Masud, Variationally derived interface stabilization for discrete multiphase flows and relation with the ghost-penalty method, *Comput. Methods Appl. Mech. Engrg.* 373 (2021) 113404, <http://dx.doi.org/10.1016/j.cma.2020.113404>.
- [48] C.R. Doering, J.D. Gibbon, *Applied Analysis of the Navier–Stokes Equations*, in: Cambridge Texts in Applied Mathematics, Cambridge University Press, 1995, <http://dx.doi.org/10.1017/CBO9780511608803>.
- [49] T.J.R. Hughes, L.P. Franca, A new finite element formulation for computational fluid dynamics: VII. The Stokes problem with various well-posed boundary conditions: Symmetric formulations that converge for all velocity/pressure spaces, *Comput. Methods Appl. Mech. Engrg.* 65 (1) (1987) 85–96, [http://dx.doi.org/10.1016/0045-7825\(87\)90184-8](http://dx.doi.org/10.1016/0045-7825(87)90184-8).
- [50] A. Masud, R. Khurram, A multiscale finite element method for the incompressible Navier–Stokes equations, *Comput. Methods Appl. Mech. Engrg.* 195 (13–16) (2006) 1750–1777, <http://dx.doi.org/10.1016/j.cma.2005.05.048>.

- [51] T.J. Hughes, *The Finite Element Method: Linear Static and Dynamic Finite Element Analysis*, Courier Corporation, 2012.
- [52] K.E. Jansen, C.H. Whiting, G.M. Hulbert, A generalized- α method for integrating the filtered Navier–Stokes equations with a stabilized finite element method, *Comput. Methods Appl. Mech. Engrg.* 190 (3) (2000) 305–319, [http://dx.doi.org/10.1016/S0045-7825\(00\)00203-6](http://dx.doi.org/10.1016/S0045-7825(00)00203-6).
- [53] A. Masud, R.A. Khurram, A multiscale/stabilized finite element method for the advection–diffusion equation, *Comput. Methods Appl. Mech. Engrg.* 193 (21–22) (2004) 1997–2018, <http://dx.doi.org/10.1016/j.cma.2003.12.047>.
- [54] S. Balay, S. Abhyankar, M.F. Adams, J. Brown, P. Brune, K. Buschelman, L. Dalcin, A. Dener, V. Eijkhout, W.D. Gropp, D. Karpeyev, D. Kaushik, M.G. Knepley, D.A. May, L.C. McInnes, R.T. Mills, T. Munson, K. Rupp, P. Sanan, B.F. Smith, S. Zampini, H. Zhang, H. Zhang, PETSc web page, 2019, <https://www.mcs.anl.gov/petsc>.
- [55] I.V. Miroshnichenko, M.A. Sheremet, Turbulent natural convection heat transfer in rectangular enclosures using experimental and numerical approaches: A review, *Renew. Sustain. Energy Rev.* 82 (2018) 40–59, <http://dx.doi.org/10.1016/j.rser.2017.09.005>.
- [56] D.R. Chenoweth, S. Paolucci, Natural convection in an enclosed vertical air layer with large horizontal temperature differences, *J. Fluid Mech.* 169 (1986) 173–210, <http://dx.doi.org/10.1017/S0022112086000587>.
- [57] C. Zhuo, C. Zhong, LES-based filter-matrix lattice Boltzmann model for simulating turbulent natural convection in a square cavity, *Int. J. Heat Fluid Flow* 42 (2013) 10–22, <http://dx.doi.org/10.1016/j.ijheatfluidflow.2013.03.013>.
- [58] P. Le Quéré, Accurate solutions to the square thermally driven cavity at high Rayleigh number, *Comput. & Fluids* 20 (1) (1991) 29–41, [http://dx.doi.org/10.1016/0045-7930\(91\)90025-D](http://dx.doi.org/10.1016/0045-7930(91)90025-D).
- [59] G. Barakos, E. Mitsoulis, D. Assimacopoulos, Natural convection flow in a square cavity revisited: Laminar and turbulent models with wall functions, *Internat. J. Numer. Methods Fluids* 18 (7) (1994) 695–719, <http://dx.doi.org/10.1002/flid.1650180705>.
- [60] J. Salat, S. Xin, P. Joubert, A. Sergent, F. Penot, P. Le Quéré, Experimental and numerical investigation of turbulent natural convection in a large air-filled cavity, *Int. J. Heat Fluid Flow* 25 (5) (2004) 824–832, <http://dx.doi.org/10.1016/j.ijheatfluidflow.2004.04.003>.
- [61] J.D. Scheel, M.S. Emran, J. Schumacher, Resolving the fine-scale structure in turbulent Rayleigh–Bénard convection, *New J. Phys.* 15 (11) (2013) 113063, <http://dx.doi.org/10.1088/1367-2630/15/11/113063>.
- [62] Y. Zhou, Rayleigh–Taylor and Richtmyer–Meshkov instability induced flow, turbulence, and mixing. I, *Phys. Rep.* 720–722 (2017) 1–136, <http://dx.doi.org/10.1016/j.physrep.2017.07.005>.
- [63] P. Erhard, D. Etling, U. Müller, U. Riedel, K. Sreenivasan, J. Warnatz, *Prandtl-Essentials of Fluid Mechanics*, Vol. 158, Springer Science & Business Media, 2010, <http://dx.doi.org/10.1007/978-1-4419-1564-1>.
- [64] J.W. Strutt, Investigation of the character of the equilibrium of an incompressible heavy fluid of variable density, *Sci. Pap.* (1900) 200–207.
- [65] W.H. Cabot, A.W. Cook, Reynolds number effects on Rayleigh–Taylor instability with possible implications for type Ia supernovae, *Nat. Phys.* 2 (8) (2006) 562–568, <http://dx.doi.org/10.1038/nphys361>.
- [66] Y. Zhou, Rayleigh–Taylor and Richtmyer–Meshkov instability induced flow, turbulence, and mixing. II, *Phys. Rep.* 723–725 (2017) 1–160, <http://dx.doi.org/10.1016/j.physrep.2017.07.008>.
- [67] Q. Zhou, Temporal evolution and scaling of mixing in two-dimensional Rayleigh–Taylor turbulence, *Phys. Fluids* 25 (8) (2013) 085107, <http://dx.doi.org/10.1063/1.4818554>.
- [68] T.T. Clark, A numerical study of the statistics of a two-dimensional Rayleigh–Taylor mixing layer, *Phys. Fluids* 15 (8) (2003) 2413–2423, <http://dx.doi.org/10.1063/1.1589015>.
- [69] G. Boffetta, F. De Lillo, A. Mazzino, S. Musacchio, Bolgiano scale in confined Rayleigh–Taylor turbulence, *J. Fluid Mech.* 690 (2012) 426–440, <http://dx.doi.org/10.1017/jfm.2011.446>.
- [70] Q. Zhou, J.R. Taylor, C.P. Caulfield, Self-similar mixing in stratified plane Couette flow for varying Prandtl number, *J. Fluid Mech.* 820 (2017) 86–120, <http://dx.doi.org/10.1017/jfm.2017.200>.
- [71] C.A. Vreugdenhil, J.R. Taylor, Large-eddy simulations of stratified plane Couette flow using the anisotropic minimum-dissipation model, *Phys. Fluids* 30 (8) (2018) 085104, <http://dx.doi.org/10.1063/1.5037039>.
- [72] R. Calderer, *Residual-Based Turbulence Models for Incompressible Flows in Domains with Moving Boundaries* (Ph.D. thesis), University of Illinois at Urbana-Champaign, 2012.